TAMPEREEN TEKNILLINEN YLIOPISTO

Roope Siikanen

ROLE OF RESONANCES AND LOCAL FIELDS IN SECOND-ORDER NONLINEAR RESPONSE OF NANOSTRUCTURES

Master of Science Thesis

Examiners: Dr. Robert Czaplicki and Prof. Martti Kauranen
Examiners and topic approved by the Faculty Council of the Faculty of Science and Environmental Engineering on 4th September 2013

ABSTRACT

TAMPERE UNIVERSITY OF TECHNOLOGY
Degree programme of Science and Engineering
SIIKANEN, ROOPE: Role of Resonances and Local Fields in Second-order Nonlinear Response of Nanostructures
Master of Science Thesis, 57 pages
November 2013
Major subject: Engineering Physics
Examiners: Dr. Robert Czaplicki and Prof. Martti Kauranen
Keywords: nanoparticles, plasmon resonances, second-harmonic generation, local fields

Metallic nanoparticles can be used to create artificial structures known as metamaterials. They possess unique physical properties not observed in nature and enable novel applications such as superlenses breaking the diffraction limit, nanoscale optical antennas and optical cloaking. In the study of nonlinear optics metamaterials are interesting since they can exhibit strong local fields to enhance nonlinear effects. Metamaterials can also be fabricated with broken symmetries to enable even-order nonlinear effects such as second-harmonic generation (SHG) which cannot occur in centrosymmetric media such as most natural materials.

In this work arrays of L- and T-shaped gold nanoparticles are studied. The shapes have one symmetry plane and are not centrosymmetric so that SHG can occur in the samples. Linear extinction spectra were measured to find the plasmon resonances which are known to enhance nonlinear effects at resonant wavelengths. Then, a laser closely matching the resonance wavelength was used to produce SHG from the samples. The studied particles are dichroic which means that the light polarization state plays a large role in the measurements. In addition to experimental work numerical simulations were ran to back up the results.

According to the results the SHG signal level cannot be predicted purely by looking at the symmetry and resonances of the samples. It was expected that any allowed SHG component with which the sample is resonant should yield a strong SHG signal. However, we measured multiple cases where these conditions were met but the signal was still weak. In addition, strong SHG signals were measured with unexpected polarization combinations. Some of these issues could be explained with the local-field simulations.

Further research on the subject is required for better understanding of the properties of these types of nanoparticle arrays. Future plans include studying particle designs with nm-scale gaps between the particles, new particle shapes and passive elements fabricated within the designs.

TIIVISTELMÄ

TAMPEREEN TEKNILLINEN YLIOPISTO
Teknis-luonnontieteellinen koulutusohjelma
SIIKANEN, ROOPE: Resonanssien ja paikalliskenttien merkitys nanorakenteiden toisen asteen epälineaarisessa optisessa vasteessa
Diplomityö, 57 sivua
Marraskuu 2013
Pääaine: Teknillinen fysiikka
Tarkastajat: Tri. Robert Czaplicki ja Prof. Martti Kauranen
Avainsanat: nanohiukkaset, plasmoniresonanssit, taajuudenkahdennus, paikalliskentät

Metallisista nanohiukkasista voidaan valmistaa keinotekoisia rakenteita, joita kutsutaan metamateriaaleiksi. Niillä on ainutlaatuisia optisia ominaisuuksia, joita ei esiinny luonnossa, ja ne mahdollistavat erikoisia sovelluksia, kuten diffraktiorajan rikkova linssi, optiset antennit ja optinen häiveteknologia. Epälineaarisessa optiikassa metamateriaalit ovat mielenkiintoisia, koska niissä esiintyy voimakkaita paikalliskenttiä, jotka vahvistavat epälineaarisia ilmiöitä. Metamateriaalit voidaan valmistaa epäsymmetrisiksi, mikä mahdollistaa parillisen asteen epälineaaristen ilmiöiden, kuten taajuudenkahdennuksen, havaitsemisen. Keskeissymmetrisissä rakenteissa, kuten useimmissa luonnollisissa materiaaleissa, näitä ilmiöitä ei esiinny.

Tässä työssä on tutkittu L- ja T-muotoisia kultananohiukkasia. Molemmilla muodoilla on yksi symmetriataso, joten keskeisymmetria on rikottu ja taajuudenkahdennus on mahdollista. Näytteiden lineaariset spektrit mitattiin plasmoniresonanssien selvittämiseksi. Näiden tiedetään voimistavan epälineaarisia ilmiöitä resonanssiaallonpituudella. Näytteistä mitattiin taajuudenkahdennusta laserilla, jonka aallonpituus on lähellä resonanssiaallonpituutta. Näytteet ovat kahtaistaittavia, joten mittauksissa käytetyn valon polarisaatiotilalla on suuri merkitys. Kokeellisen osuuden lisäksi tehtiin numeerisia simulaatioita tulosten tueksi.

Tulosten perusteella taajuudenkahdennuksen voimakkuutta ei voi ennustaa pelkästään näytteen symmetriasta ja resonansseista. Aikaisempien tutkimusten perusteella oli odotettavaa, että voimakas taajuudenkahdennussignaali havaitaan, kun käytetään sopivaa polarisaatiotilaa ja resonanssiaallonpituutta. Joissakin tapauksissa havaittiin kuitenkin vain heikkoja signaaleja, vaikka molemmat kriteerit täyttyivät. Toisaalta voimakkaita signaaleita havaittiin myös käyttäen yllättäviä polarisaatioyhdistelmiä. Havaittuja ongelmia pystyttiin osittain selittämään paikalliskenttäsimulaatioilla.

Nanorakenteiden parempi ymmärtäminen vaatii lisätutkimuksia aiheesta. Suunnitelmana on tutkia esimerkiksi rakenteita, joissa on nanometriluokan rakoja hiukkasten välillä, uusia hiukkasten muotoja ja rakenteita, joissa on mukana passiivisia hiukkasia.

FOREWORD

This work has been carried out during summer and autumn 2013 in the Optics Laboratory of Tampere University of Technology under the supervision of Dr. Robert Czaplicki and Prof. Martti Kauranen.

I want to thank my examiners for their generous support and advice concerning the work. Thank you for all your comments and corrections which have been plentiful and helpful. Also thanks to the people at the University of Eastern Finland, who have prepared the samples studied in the work. I also need to mention Jouni who has written all the codes used in the numerical simulations. Thanks for your time and advice concerning my problems using the code. At times my questions have been very stupid.

Also thanks to all the people in the lab for creating a pleasant atmosphere to work in. I specifically need to mention my office mates Mari, Liisa, Elisa and Jan; and Kalle with whom I've had so many useful conversations concerning work, and also some other stuff at times.

"It's the job that's never started as takes longest to finish."
- Samwise Gamgee / The Fellowship of the Ring -

Tampere 20.11.2013
Roope Siikanen

CONTENTS

SYMBOLS AND ABBREVIATIONS

Scalar quantities are written in *italics* (eg. x) and vector quantities in **bold** (eg. $\mathbf{E}$).

Symbols

$*$	Complex conjugate
$\otimes$	Tensor product
A	Optical density
A_{ijk}	Nonlinear response tensor
$\mathbf{B}$	Magnetic field density
C_i	Nonlinear response scaling parameter
c	Speed of light
$\mathbf{D}$	Electric displacement field
$\mathbf{E}$	Electric field
$\mathbf{H}$	Magnetic field
I	Intensity
$\mathbf{J}$	Free current density
k	Wavenumber
$\mathbf{k}$	Propagation vector
k_{SP}	Surface plasmon wavenumber
m_e	Mass of electron
N_e	Electron density
N_i	Photon number of polarization state i
n	Refractive index
$\mathbf{P}$	Polarization field
$\mathbf{P}^{(1)}$	Linear polarization field
$\mathbf{P}^{\mathrm{NL}}$	Nonlinear polarization field

$\mathbf{P}^{(n)}$	n'th order nonlinear polarization field
$\mathbf{r}$	Position vector
x, y, z	Cartesian coordinates
δ_{SP}	Surface plasmon propagation length
ϵ	Permittivity
ϵ_0	Permittivity of vacuum
$\tilde{\epsilon}$	Complex Permittivity
λ	Wavelength
μ	Permeability
ρ	Free charge density
σ	Conductivity
τ	Relaxation time
χ_e	Electric susceptibility
$\chi^{(n)}$	n'th order nonlinear susceptibility tensor
$\chi^{(n)}_{ijk}$	n'th order nonlinear susceptibility tensor component (output i, input j and k)
ω	Angular frequency
ω_p	Plasma frequency
ω_{SP}	Surface plasmon frequency

Abbreviations

BEM	Boundary element method
DFG	Difference-frequency generation
FDTD	Finite-difference time-domain
FWHM	Full-width at half maximum
HWP	Half-wave plate
IR	Infrared
LP	Linear polarizer
LSP	Localized surface plasmon
NL	Nonlinear
NLO	Nonlinear optics
NRT	Nonlinear response tensor
PMMA	Polymethyl-metacrylate
PMT	Photomultiplier tube
SEM	Scanning electron microscope
SFG	Sum-frequency generation
SHG	Second-harmonic generation
SP	Surface plasmon

1. INTRODUCTION

"We learn something every day, and lots of times it's that what we learned the day before was wrong."

- Bill Vaughan

Nowadays we are surrounded by optics. Our day to day life would be much different without optical devices ranging from simple applications such as eye glasses and camera lenses to more complex instruments like laser pointers and DVD-players. Most telecommunications nowadays is handled by optical fibers. Our reliance on these innovations makes optics an important field of research.

Nonlinear optics (NLO) is a field of optics which studies materials whose properties change when exposed to light. This makes the relation between input and response signals nonlinear and allows interesting phenomena such as self-focusing of light beams and generation of new frequencies in the output field. Usually nonlinear effects are very weak and require extremely strong electric fields and special materials to observe. Because of this it was not until the discovery of lasers that NLO effects were discovered.

Our Research Group

The Nonlinear Optics Group at Tampere University of Technology (TUT) focuses on experimental work on nonlinear optics. We research topics such as structures of metallic nanoparticles [1], nonlinear films [2], nonlinear microscopy [3, 4] and organic materials [5]. In addition some people in our group develop computational methods to simulate the experiments and generate comparable results based on theoretical models [6]. For the most part we do not prepare the materials used in experiments ourselves and collaborate with numerous other organizations who specialize in sample fabrication. At TUT these include the Aerosol Physics Group and the Optoelectronics Research Center (ORC). We also collaborate with Aalto University, University of Eastern Finland and numerous foreign universities.

Metamaterials

The project I have worked on focuses on the study of nonlinear optical properties of gold nanoparticle arrays. The work has been done in collaboration with the University of Eastern Finland at Joensuu. The studied samples are a type of *metamaterial*, which are artificially crafted media composed of nanoscale structures. Nanostructures can be fabricated using many different methods such as lithographic methods, nanoimprintation and laser beam writing [7]. Nanoparticle structures have also been created using aerosol techniques [8] and wet chemistry [9]. Aside from more conventional particle shapes such as spheres, dots and bars many exotic types of particles have been studied such as T-shaped nanodimers [10], L-shaped particles [11], split-ring resonators [12] and core-shell structures [13].

What makes metamaterials an interesting research subject is that they can possess negative permittivity and permeability which gives raise to extraordinary optical properties not observed in nature, for example negative refractive index [14]. Properties of metamaterial nanostructures can be fine-tuned in sample fabrication which makes them versatile materials. These unique properties enable many novel applications, some of which are only theoretical at the moment. Possible uses for negative-index metamaterials include creating a superlens which is predicted to break the diffraction limit in imaging [15], cloaking technologies based on bending light beams [16] and nanoscale antennas operating at optical frequencies [17].

Another important quality of metamaterials is that they can induce strong local electromagnetic fields when exposed to an external optical field. Field enhancements of several orders of magnitude have been predicted theoretically [18] but experimentally only enhancements of about 100 have been observed. These strong local fields make metamaterial structures desirable for nonlinear optics. Nonlinear effects are proportional to a higher power of the field and can be amplified in metamaterials with strong local fields.

Samples and Experiments

Our research focuses on plasmonic and nonlinear properties of nanostructures with a goal of learning to fine-tune these properties in fabrication. First we measured the linear spectra of the samples to find their resonance wavelengths. In the nonlinear experiments we measure second-harmonic generation (SHG) from the samples using an IR-laser with the wavelength of 1060 nm. The samples are designed to possess plasmonic resonances near the laser wavelength to amplify the nonlinear response. The experimental results are backed up with computational simulations using two different numerical methods, finite-difference time-domain (FDTD) method and boundary element method (BEM).

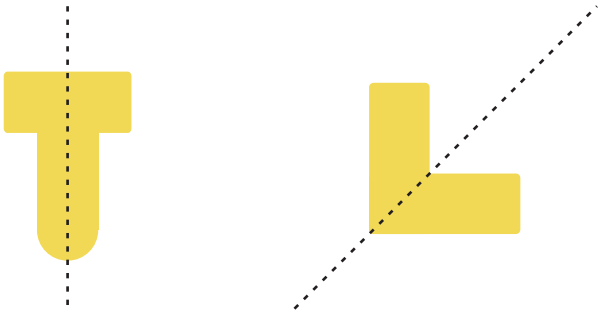

Figure 1.1: The samples studied in this work are L- and T-shaped gold nanoparticles.

Because second-order nonlinear effects cannot occur in centrosymmetric materials the samples must be designed to have broken symmetries. The samples studied in this work are arrays of L- and T-shaped particles (Fig. 1.1). The studied particles have one symmetry plane and are not centrosymmetric so can produce a SHG response even at normal incidence. The symmetry plane still influences SHG and causes certain combinations of input and output polarizations to be forbidden. The samples are strongly dichroic which means the experiments are largely influenced by the polarization states of the input and output fields.

Summary of Results

The measurements of linear extinction spectra yielded mostly expected results. We observed resonance peaks at roughly the wavelengths the samples were designed for. All the samples have resonance peaks close to our laser wavelength which has been shown to enhance nonlinear effects [19].

However, we got some unexpected results from the SHG measurements. Our prediction was that the samples should obey the SHG symmetry rules established in previous studies, stating that in order to gain a strong SHG signal the component should be allowed and the input field should match with a resonance [20]. Only the reference sample of L-particles obeyed this rule but for the T-particles we observed some such components with very weak signals. Surprisingly the strongest SHG signals were measured with a mixed input polarization not aligned with either of the main axes of the particles. This means that SHG from nanoparticle arrays cannot be predicted purely by plasmonic features but a more detailed explanation is needed.

The simulated spectra from numerical calculations were of similar form to the measured ones. Details such as exact resonance wavelengths were different which could be caused by approximations in the simulations. With the aid of the calculations we were able to clarify some issues concerning hypothesized particle shapes in

the samples. Using the local-field simulations we were able to address several issues concerning the SHG signals explain why some components produce different signals than predicted by their plasmonic properties.

Structure of Thesis

The thesis is divided into six chapters. After this introduction is a general outlook to linear and nonlinear optics. For the linear part, some central concepts in optics related to the work are discussed. The nonlinear optics chapter includes a more thorough discussion about SHG and metal nanoparticles. In Chapter 4, I will explain the methods used in the experiments and numerical calculations. Chapter 5 features the experimental results and discussion and Chapter 6 has a summary and final conclusion about the work.

2. OPTICS

"Light is something like raindrops - each little lump of light is called a photon - and if the light is all one color, all the "raindrops" are the same."

- Richard Feynman

Optics is the branch of physics that studies the properties of light and interactions between light and matter. Light can be described as wave motion of electric and magnetic fields or as massless particles called photons [21, p. 37]. In optics, the most common approach is to describe light as an electromagnetic wave.

Frequency Components of Light

A monochromatic harmonic plane wave can be written as

$$\mathbf{E}(\mathbf{r}, t) = \mathbf{E_0} e^{i(\mathbf{k}\cdot\mathbf{r} - \omega t)}\,, \tag{2.1}$$

where $\mathbf{E_0}$ is the vector amplitude of the electric field associated with the wave, $\mathbf{k}$ is the propagation vector, $\mathbf{r}$ is the position vector and ω is the angular frequency of the wave. Usually it is possible to use a coordinate system in which the wave propagates in the direction of one of the coordinate axes. In this case one can use a simpler form

$$\mathbf{E}(z, t) = \mathbf{E_0} e^{i(kz - \omega t)}\,, \tag{2.2}$$

where the propagation vector $\mathbf{k}$ is replaced with the scalar propagation number k, also called wavenumber, and the position vector $\mathbf{r}$ is replaced by the z-coordinate, describing a wave propagating in the z-direction.

Most light is not monochromatic but contains components at multiple wavelengths. It is often more convenient to describe the fields associated with light in the frequency domain rather than time domain. In general optical phenomena are wavelength dependent which makes the frequency component approach easier for many situations. A time-dependent electric field expanded in terms of its frequency

components is written as

$$\mathbf{E}(\mathbf{r},t) = \sum_{n=-\infty}^{\infty} \mathbf{E}(\mathbf{r},\omega_n)e^{-i\omega_n t}\,, \tag{2.3}$$

where $\mathbf{E}(\mathbf{r},\omega_n)$ is the component of the field corresponding to frequency ω_n. The frequencies in the expression can be negative which is a result of mathematical notation. To ensure that the total fields are real, the frequency component associated with the negative frequency $-\omega$ must be the complex conjugate of the corresponding frequency component associated with frequency ω

$$\mathbf{E}(\mathbf{r},-\omega_n) = \mathbf{E}^*(\mathbf{r},\omega_n)\,. \tag{2.4}$$

When frequency components associated with ω and $-\omega$ are summed, the total field is real valued.

Index of Refraction

In vacuum light propagates at the speed of light c. However, when light passes through a medium its velocity changes depending on the material. This effect is described with the index of refraction n of the material which is defined as

$$n = c/v\,, \tag{2.5}$$

where v is the velocity of light in the material. In the case of air the velocity of light is almost unchanged which means that air has a refractive index of $n \approx 1$. In transparent liquids and solids light is slowed down and the value of the index of refraction is higher. Generally the index of refraction is also a function of the wavelength of light. This effect is called dispersion.

The previous simple description is only valid for transparent materials like glass where most of the light propagates through the medium. For opaque materials part of the light is absorbed or scattered which is described by the imaginary part of the refractive index. For metals, this imaginary part is a result of conductivity of the medium. Thus in the general case the index of refraction $\tilde{n}$ is a complex quantity which can be written as [21, p. 127]

$$\tilde{n} = n_{\mathrm{R}} + in_{\mathrm{I}}\,, \tag{2.6}$$

where n_{R} and n_{I} are the real and imaginary parts of the refractive index. For transparent materials the imaginary part is vanishingly small and the index of refraction can be taken to be real-valued.

A plane wave propagating in z-direction within a medium with a complex index of refraction is written as

$$\mathbf{E}(z,t) = \mathbf{E_0} e^{i(\tilde{n}kz - \omega t)} . \tag{2.7}$$

When we substitute into this equation the complex index of refraction given by Equation (2.6) and separate the real and imaginary parts the wave can be written in form

$$\mathbf{E}(z,t) = \mathbf{E_0} e^{-n_{\mathrm{I}}kz} e^{i(n_{\mathrm{R}}kz - \omega t)} . \tag{2.8}$$

The latter exponential has the form of harmonic wave motion which is the same as before, while the first exponential represents exponential decay. A nonzero imaginary part of refractive index thus leads to absorption in the material and exponential damping of the field as a function of distance. Most opaque materials, especially metals are highly absorptive and have a complex index of refraction at optical frequencies.

Polarization

The direction of the electric field $\mathbf{E}$ determines the polarization state of light. A light wave written as in Equation (2.2) is said to be *linearly polarized*. For linearly polarized light the associated electric field varies only in strength but not in direction. The electric field oscillates in a plane. Two other common polarization states are *circular* and *elliptical* polarization (Fig. 2.1).

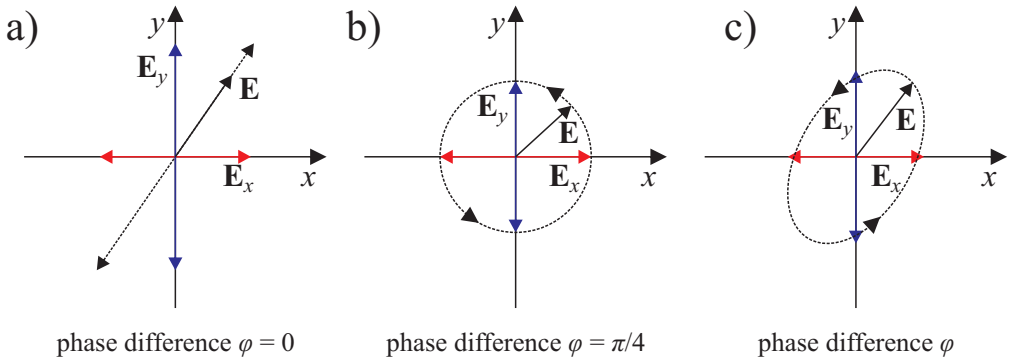

Figure 2.1: Examples of a) linear, b) circular and c) elliptical polarization. Light propagates in positive z-direction, out of the plane.

For circularly polarized light the electric field vector has constant value and rotates around the optical axis. The end point of the field vector follows a circle when viewed along the direction of propagation. Circularly polarized light can be generated with two linearly polarized fields with equal amplitude perpendicular to each other and with a $\pi/4$ phase difference. This is most commonly achieved using a quarter-wave plate. Similar to the latter is elliptical polarization, but the electric

field vector follows an elliptical curve. Elliptically polarized light can be generated in the same way as circular, except that the amplitudes and phase differences of the two components are arbitrary. So, linear and circular polarizations are special cases of elliptical polarization. Light from most natural light sources such as broadband bulbs or daylight is unpolarized and contains linearly oscillating fields in all directions.

There are also more exotic polarization states, such as radial and azimuthal polarization which describe light beams that have different polarization states in different parts of the beam. In this work only linear polarization is considered.

2.1 Maxwell Equations

As an electromagnetic wave, light can be described by the Maxwell Equations. They can be written in differential form using Gaussian units as follows [22, p. 68]:

$$\nabla \cdot \mathbf{D} = 4\pi\rho \tag{2.9}$$

$$\nabla \cdot \mathbf{E} = 0 \tag{2.10}$$

$$\nabla \times \mathbf{E} = -\frac{1}{c}\frac{\partial \mathbf{B}}{\partial t} \tag{2.11}$$

$$\nabla \times \mathbf{H} = \frac{1}{c}\frac{\partial \mathbf{D}}{\partial t} + \frac{4\pi}{c}\mathbf{J}\,. \tag{2.12}$$

The meanings of the symbols in the equations are as follows: $\mathbf{D}$ - electric displacement field, ρ - free charge density, $\mathbf{B}$ - magnetic field density, $\mathbf{E}$ - electric field, c - speed of light, $\mathbf{H}$ - magnetic field, $\mathbf{J}$ - free current density. The fields and quantities involved in the equations are also related by material equations. For an isotropic medium they take the following form:

$$\mathbf{J} = \sigma\mathbf{E} \tag{2.13}$$

$$\mathbf{D} = \epsilon\mathbf{E} \tag{2.14}$$

$$\mathbf{B} = \mu\mathbf{H}\,. \tag{2.15}$$

In these equations, σ is the conductivity, ϵ - the permittivity and μ - the permeability of the material. In the general case all the material parameters are wavelength dependent. The relation between fields $\mathbf{E}$ and $\mathbf{D}$ can also be expressed using the electric polarization of the material $\mathbf{P}$ as follows

$$\mathbf{D} = \mathbf{E} + 4\pi\mathbf{P}\,. \tag{2.16}$$

The polarization depends on the electric field $\mathbf{E}$ through the equation

$$\mathbf{P} = \chi_e \mathbf{E}\,, \tag{2.17}$$

where χ_e represents the electric susceptibility of the material. In the most general case χ_e is a tensor quantity. Similar to the electric field the polarization can be expanded in terms of frequency components

$$\mathbf{P}(\mathbf{r},t) = \sum_{n=-\infty}^{\infty} \mathbf{P}(\mathbf{r},\omega_n) e^{-i\omega_n t}\,. \tag{2.18}$$

Within the linear approximation the material polarization has the same frequency components as the optical field, but nonlinearity can give raise to new frequencies in the polarization.

Wave Equation

As an electromagnetic wave light must satisfy a wave equation which can be derived from the Maxwell equations. Let's consider a case of no free charges ($\rho = 0$), no free currents ($\mathbf{J} = 0$) and nonmagnetic material ($\mathbf{B} = \mathbf{H}$). Let's also assume an isotropic and homogeneous medium. Begin with taking a curl from Faraday's law (2.11) and substituting into material equation (2.15)

$$\nabla \times (\nabla \times \mathbf{E}) = -\nabla \times \frac{1}{c}\frac{\partial \mathbf{H}}{\partial t}\,. \tag{2.19}$$

The differentials on the right-hand side are linear operations so we can switch their order and apply Ampère's law (2.12). Because we assumed a nonconducting material, the term $\frac{4\pi}{c}\mathbf{J}$ on the right hand side is zero. Also we can use the vector identity

$$\nabla \times (\nabla \times \mathbf{F}) = \nabla(\nabla \cdot \mathbf{F}) - \nabla^2 \mathbf{F} \tag{2.20}$$

to simplify the left-hand side. Applying these steps yields the equation

$$\nabla(\nabla \cdot \mathbf{E}) - \nabla^2 \mathbf{E} = -\frac{1}{c^2}\frac{\partial^2 \mathbf{D}}{\partial t^2}\,. \tag{2.21}$$

In the case of homogeneous and isotropic medium the divergence of the electric field must be zero. This eliminates the term $\nabla(\nabla \cdot \mathbf{E})$ on the left-hand side. By substituting equation (2.16) into (2.21), we get the result

$$\nabla^2 \mathbf{E} = \frac{1}{c^2}\frac{\partial^2 \mathbf{E}}{\partial t^2} + \frac{4\pi}{c^2}\frac{\partial^2 \mathbf{P}}{\partial t^2} \tag{2.22}$$

which is the wave equation for electromagnetic radiation. In nonlinear optics $\nabla \cdot \mathbf{E}$ is nonzero even in the case of isotropic materials. However, it can be shown to be small and thus neglected from the equation even in the nonzero case in most cases of practical interest [22, p. 69-70]. A wave equation of equal form can be derived for the magnetic field. Because the electric and magnetic fields are connected through the Maxwell equations it is sufficient to only consider the electric field when describing light.

For a harmonic plane wave, the solution to the wave equation can be further simplified. For a harmonic wave, taking the second derivative with respect to time is equivalent to multiplication by ω^2. We can apply this simplification separately to all frequency components which yields

$$\nabla^2 \mathbf{E}(\omega_n) = \frac{\omega_n^2}{c^2}\mathbf{E}(\omega_n) + \frac{4\pi\omega_n^2}{c^2}\mathbf{P}(\omega_n)\,. \tag{2.23}$$

Light in a Conducting Medium

The previous treatment only works for dielectric materials. For conducting materials such as the metallic nanoparticles studied in this work the assumption of $\mathbf{J} = 0$ is not valid and the wave equation must be modified accordingly. In conducting materials the second term on the right-hand side of Ampère's law is not zero which adds an extra term to equation (2.21)

$$\nabla^2 \mathbf{E} = \frac{1}{c^2}\frac{\partial^2 \mathbf{D}}{\partial^2 t} + \frac{4\pi}{c^2}\frac{\partial \mathbf{J}}{\partial t}\,. \tag{2.24}$$

Apply the material equations (2.14, 2.15) and we get the wave equation for conducting materials

$$\nabla^2 \mathbf{E} = \frac{\epsilon}{c^2}\frac{\partial^2 \mathbf{E}}{\partial^2 t} + \frac{4\pi\sigma}{c^2}\frac{\partial \mathbf{E}}{\partial t}\,. \tag{2.25}$$

From equation (2.25) can be derived the expression for the complex permittivity $\tilde{\epsilon}$ [23, p. 613]

$$\tilde{\epsilon} = \epsilon + i\frac{4\pi\sigma}{\omega}\,. \tag{2.26}$$

The dielectric constant is related to the index of refraction and thus a complex dielectric constant results in a complex index of refraction which in turn leads to absorption losses in the material. For dielectric materials, on the other hand, the conductivity σ is almost zero which means that their refractive indices are essentially real.

2.2 Scattering of Light

In general, scattering is a physical process in which light or a stream of particles deviates from straight propagation. Scattering is caused by heterogeneity of materials. All media besides vacuum scatter light since at the microscopic scale all matter is formed of individual particles which comprises a heterogeneous medium. Scattering of light at the microscopic level is the fundamental cause for many macroscopic optical phenomena. For example, reflection, refraction and diffraction of light beams are all results of light scattering at interfaces between materials [24, p. 4].

Scattering can be divided into two cases: elastic and inelastic. In elastic scattering energy is conserved and all energy in the incident field is radiated away from the scattering medium. In inelastic scattering part of the field energy is lost to the scatterer and turned into heat for example. This is observed as a change in the wavelength of the scattered field.

The simplest way to describe electromagnetic scattering is the Lorentz model for a single charged particle, like an electron. When the electric field associated with incident light interacts with the electron, an electric force is applied on the electron. The electron is forced into harmonic motion driven by the field. The theory of electromagnetism states that accelerating charges radiate electromagnetic radiation and so the electron emits light at the same frequency as the driving field. This oscillation creates a varying charge density within the medium which can be approximated as an effective dipole. Thus the scattered field has the profile of dipole radiation which means that the scattered field is mostly radiated in directions perpendicular to the oscillation of the electron.

In reality we never observe scattering from just a single electric dipole. Materials can be divided into small regions and the incident light induces dipoles to form in each of them. The total scattered field is the superposition of the scattered fields from all induced dipoles. In general the dipoles are electromagnetically coupled: the scattered fields from the dipoles interact with and scatter from other dipoles. This means that calculations involving multiple dipoles can become extremely complex. However, in several cases approximations with individual decoupled dipoles yield sufficient results.

When observing light beams propagating through a scattering medium scattering acts as a loss mechanism similar to absorption. Part of the incident beam is scattered in all directions and the signal in the original beam direction is weakened. With the simplest measurement setups it is not possible to distinguish losses caused by absorption from those caused by scattering. When the actual loss mechanism is not relevant, scattering and absorption can be treated together as one loss mechanism. The combined loss due to scattering and absorption is called *extinction*.

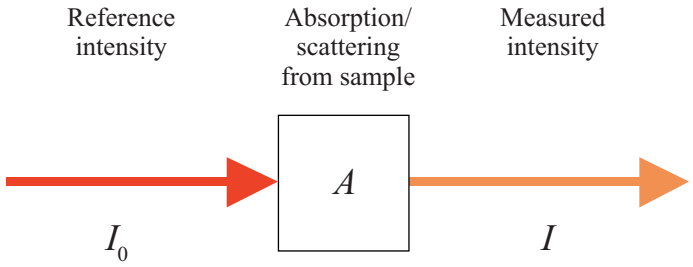

Figure 2.2: Measuring optical density of a sample.

Quantitatively extinction losses can be described by the *optical density* A, also sometimes called *absorbance* [25, p. 33]. Optical density is generally dependent on wavelength and is defined as

$$A(\lambda) = -\log_{10}\left(\frac{I(\lambda)}{I_0(\lambda)}\right), \tag{2.27}$$

where I_0 is the incident intensity (reference intensity) and I is light intensity after propagating through the sample (Fig. 2.2). If the studied sample is fabricated on the surface of a substrate such as glass, the reference intensity is usually measured through the substrate to neglect any effects from the substrate.

3. NONLINEAR OPTICS

"Everything should be made as simple as possible, but no simpler."
- Albert Einstein

Nonlinear optics studies phenomena where the optical properties of materials change when exposed to strong electric fields associated with light. The relation between the incident field strength and optical response in such materials is nonlinear. Actually all physical phenomena are nonlinear but in general nonlinear effects are very weak and observing them requires extreme conditions. As such, linear approximations are valid for most engineering problems.

In optics, observing nonlinear effects requires high field strengths which can be achieved with (pulsed) lasers. The research of nonlinear optics began soon after the emergence of first lasers in 1960 and the first observation of second-harmonic generation of light by Franken and co-workers occurred in 1961 [26]. Nowadays devices based on NLO effects are used in everyday life and industry. Applications include generating light with a higher frequency, self-focusing materials and optical modulators. The most common everyday device based on NLO is the green laser pointer. Its light output is created by frequency doubling the light of an infrared laser with a NL crystal.

Nonlinear Wave Equation

In nonlinear optics, the relation between the incident optical field and material response in equation (2.17) is taken to be nonlinear. The polarization $\mathbf{P}$ can be expressed as a sum of the linear part $\mathbf{P}^{(1)}$ and the nonlinear part $\mathbf{P}^{\mathrm{NL}}$

$$\mathbf{P} = \mathbf{P}^{(1)} + \mathbf{P}^{\mathrm{NL}} \tag{3.1}$$

which means that we can write a new relation between the fields $\mathbf{D}$ and $\mathbf{E}$

$$\begin{aligned} \mathbf{D} &= \mathbf{E} + 4\pi(\mathbf{P}^{(1)} + \mathbf{P}^{\mathrm{NL}}) \\ &= \epsilon^{(1)}\mathbf{E} + 4\pi \boldsymbol{P}^{\mathrm{NL}}\,, \end{aligned} \tag{3.2}$$

where $\epsilon^{(1)}$ is the linear permittivity of the medium. This can be substituted into the previously derived wave equation (2.21) which yields the result

$$\nabla^2\mathbf{E} = \frac{\epsilon^{(1)}}{c^2}\frac{\partial^2\mathbf{E}}{\partial^2 t} + \frac{4\pi}{c^2}\frac{\partial^2\mathbf{P}^{\mathrm{NL}}}{\partial^2 t}\,. \tag{3.3}$$

We can apply this equation to the monochromatic case where we can take the time derivatives from each frequency component separately. The nonlinear wave equation in this case can be written as [22, p. 71]

$$\nabla^2\mathbf{E}(\mathbf{r},\omega_n) = \frac{\omega_n^2\epsilon^{(1)}(\omega_n)}{c^2}\mathbf{E}(\mathbf{r},\omega_n) + \frac{4\pi\omega_n^2}{c^2}\mathbf{P}^{\mathrm{NL}}(\mathbf{r},\omega_n)\,, \tag{3.4}$$

where $\epsilon^{(1)}(\omega_n)$ emphasizes that the permittivity of the material varies with frequency.

3.1 Nonlinear Susceptibility

The exact functional form of the nonlinear part of material polarization $\mathbf{P}^{(NL)}$ can be very complex so most often it is necessary to use approximations. The most commonly used nonlinear approximation is to expand the material response as a power series in terms of the optical field. The series can be taken to be convergent which means that the higher-order susceptibilities rapidly get weaker with rising order. In the power series expansion the material polarization can be written as a function of $\mathbf{E}$

$$\mathbf{P}(\mathbf{r},t) = \sum_i \chi^{(i)}(\mathbf{r},t)\otimes\mathbf{E}^i(\mathbf{r},t)\,, \tag{3.5}$$

where $\chi^{(i)}$ is the nonlinear susceptibility tensor of i:th order and $\otimes$ denotes tensor product. The susceptibilities are tensor quantities and as a general rule the susceptibility $\chi^{(i)}$ has to be a $(i+1)$ rank tensor [22, p. 2]. In this work only nonlinear effects of second order are taken into account. The second-order polarization term can be written in terms of cartesian and frequency components as

$$P_i^{(2)}(\mathbf{r},\omega_m+\omega_n) = \sum_{jk}\sum_{(mn)}\chi_{ijk}^{(2)}(\mathbf{r},\omega_m+\omega_n;\omega_m,\omega_n)E_j(\mathbf{r},\omega_m)E_k(\mathbf{r},\omega_n)\,, \tag{3.6}$$

where the indices i,j,k refer to the cartesian coordinates of the fields and m,n to frequency components of the optical field. The notation (mn) emphasizes that the sum $\omega_m+\omega_n$ is held fixed while ω_m and ω_n may vary. This is a result of the fact that energy must be conserved. The summation indices j and k carry out over the three cartesian coordinates.

In this work, we only consider nonlinear polarization due to electric dipoles. Within this approximation the susceptibility tensor can be taken to be independent

of position **r** [27, p. 5] which means that we can drop the position arguments from equation (3.6) from now on

$$P_i^{(2)}(\omega_m + \omega_n) = \sum_{jk} \sum_{(mn)} \chi_{ijk}^{(2)}(\omega_m + \omega_n; \omega_m, \omega_n) E_j(\omega_m) E_k(\omega_n) \,. \tag{3.7}$$

3.2 Second-harmonic Generation

The second-order polarization in equation (3.6) is related to the product of the optical fields $E(\omega_m)E(\omega_n)$. This product has a time dependence of form $e^{-i(\omega_m+\omega_n)t}$ which means that the nonlinear polarization oscillates at a frequency which is the sum of the frequencies of the two optical fields. This phenomenon is known as *sum-frequency generation* (SFG) [22, p. 19]. By taking into account the complex conjugates of the fields, which are expressed as negative frequencies, a phenomenon known as *difference-frequency generation* (DFG) can be observed. In this case, frequencies that are equal to differences between ω_m and ω_n are generated. Energy level diagrams for different nonlinear phenomena are illustrated in figure 3.1.

An important case of sum-frequency generation is *second-harmonic generation* (SHG) in which both incident fields have the same frequency ω. This is the simplest case to study because SHG can be observed with just a monochromatic laser and a nonlinear medium. In SHG the second-order polarization oscillates at frequency 2ω, producing light with doubled frequency and halved wavelength, which is why the phenomenon is also called *frequency doubling*. The second order polarization for SHG can be written as

$$P_i^{(2)}(2\omega) = \sum_{jk} \chi_{ijk}^{(2)}(2\omega; \omega, \omega) E_j(\omega) E_k(\omega) \,. \tag{3.8}$$

In the most general case the product of fields in the equation cannot be written as E^2 because E_j and E_k can still have different polarization states.

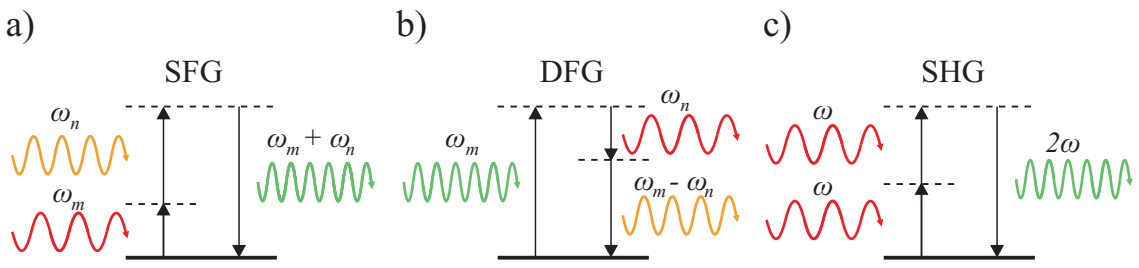

Figure 3.1: Energy level diagrams for a) SFG, b) DFG and c) SHG. ω_m, ω_n and ω are the frequencies of input photons.

The total SHG signal from a NL medium is a superposition of all SHG fields

generated from all parts of the medium. The SHG fields tend to interfere destructively unless phase-matching is achieved and in consequence the SHG signal cannot become strong. When phase matching conditions are met, strong SHG fields can be achieved. This means that SHG is highly sensitive to phases of input fields.

Symmetry and SHG

The second-order susceptibility tensor $\chi^{(2)}$ has 27 components. However, not all of these are independent since symmetries can force certain components to be equal. One such symmetry is caused by the fact that the incident photons are indistinguishable and their order can be switched freely. The indices j and k can be permutated along with their frequency arguments. This results in the intrinsic symmetry relation

$$\chi^{(2)}_{ijk}(\mathbf{r}, \omega_m + \omega_n; \omega_m, \omega_n) = \chi^{(2)}_{ikj}(\mathbf{r}, \omega_m + \omega_n; \omega_n, \omega_m) \tag{3.9}$$

which is always valid since the order of the photons is just a mathematical notation.

Another kind of symmetry arises when we consider a material with no resonances at the field frequency. In this case the material can be assumed to be lossless and the susceptibility to be independent of frequency. This leads to Kleinmann symmetry, which means that both the frequency arguments and cartesian indices can be freely permuted

$$\chi^{(2)}_{ijk} = \chi^{(2)}_{ikj} = \chi^{(2)}_{jik} = \chi^{(2)}_{kij} = \chi^{(2)}_{jki} = \chi^{(2)}_{kji}\,. \tag{3.10}$$

An important class of symmetry regarding SHG is centrosymmetry, which means that the material has a center of inversion. For centrosymmetric materials the following transformations are valid

$$\begin{aligned} \mathbf{r} &\rightarrow -\mathbf{r} \\ \mathbf{E} &\rightarrow -\mathbf{E} \\ \mathbf{P} &\rightarrow -\mathbf{P}\,. \end{aligned}$$

When these are applied to the nonlinear polarization term

$$\mathbf{P}^{(2)}(2\omega) = \chi^{(2)}(2\omega; \omega, \omega) \otimes (\mathbf{E}(\omega))^2\,, \tag{3.11}$$

we obtain

$$\begin{aligned} -\mathbf{P}^{(2)}(2\omega) &= \chi^{(2)}(2\omega; \omega, \omega) \otimes (-\mathbf{E}(\omega))^2 \\ &= \chi^{(2)}(2\omega; \omega, \omega) \otimes (\mathbf{E}(\omega))^2 \\ &= \mathbf{P}^{(2)}(2\omega)\,, \end{aligned} \tag{3.12}$$

which can only be valid if $\chi^{(2)}(2\omega;\omega,\omega)$ is identically zero. This means that centrosymmetric materials cannot have a second-order nonlinear response and a way to break material symmetry needs to be devised to observe second-order nonlinear phenomena. However, materials are never perfectly symmetric and any defects or impurities will give rise to nonlinear effects. Interfaces and surfaces between materials also naturally break the symmetry which means that SHG is often primarily a surface effect. This sensitivity makes SHG an effective tool for examining the properties of materials.

3.3 Metal Nanoparticles

Metallic structures with dimensions below the wavelength of visible light are a topic of great interest in the field of optics. Nanoscale particles with sizes ranging from few to hundreds of nm have unique properties in their interaction with light, such as a negative index of refraction [28]. Metallic nanoparticles have been used since ancient times to decorate windows and glass ornaments with various colours. Nowadays we know more about their interaction with light and nanoparticles of different sizes and shapes can be artificially crafted. Nanoparticles can be used as building blocks for *metamaterials* [29,30], which are artificial materials with unique physical properties [31, p. xiii]. Modern fabrication processes allow for precise detail in particle shape which means that the optical properties of nanoparticle metamaterials can be fine-tuned by altering fabrication parameters.

Plasmons

The optical properties of metals are tied to their electron structure. A commonly used model for metals is the free electron gas, where the valence electrons of metal atoms move freely in a lattice formed by the positively charged metallic ions [32, p. 137]. An electric field applied to the electron gas can induce charge density oscillations, also called plasma oscillations, within the material. These oscillations are quantized and the quanta of them are called *plasmons*.

The frequency of plasma oscillations ω_p, called the *plasma frequency*, can be written as [32, p. 142]

$$\omega_p = \frac{N_e e^2}{\epsilon_0 m_e}, \tag{3.13}$$

where N_e is the electron density, ϵ_0 the permittivity of a vacuum and m_e the mass of an electron. The plasma frequency of a material influences its optical response. An expression for the refractive index of free electron gas can be derived from the Maxwell's equations. For nonmagnetic materials the refractive index can be written

as [32, p. 158]

$$n^2 = 1 - \frac{\omega_p^2}{\omega^2 + i\omega/\tau}\,, \tag{3.14}$$

where τ is the relaxation time of the electron gas. The relaxation time is related to the time between collisions of electrons in the free electron gas. For noble metals with high conductivity, such as gold, τ can be assumed to be very large and the second term in the denominator can be dropped

$$n^2 = 1 - \frac{\omega_p^2}{\omega^2}\,. \tag{3.15}$$

Depending on the ratio ω_p^2/ω^2 the index of refraction can be either purely real or purely imaginary. For frequencies below the plasma frequency the material is transparent while for higher frequencies is is absorptive.

The above description does not take into account any effects of boundaries and interfaces in the material. Plasmons described as such are called *bulk plasmons* which are electric oscillations in the bulk material, far from any edges and interfaces. Bulk plasmons are longitudinal oscillations and they cannot interact with light which is a transverse wave.

Surface Plasmons

When charge density oscillations occur near interfaces between conductors and dielectric materials, they are called *surface plasmons* (SP). SPs have lower frequencies than bulk plasmons and oscillate along the surface. They can also couple with light under certain conditions. SPs were first observed by Powell and Swan [33] through study of thin metal films and observation of energy losses smaller than bulk plasmon energy.

SPs are essentially waves propagating along the metallic surface and interact with the conducting electrons, giving raise to a resonant oscillation [34]. However, not all surfaces support surface plasmon modes. The criterion for surface plasmons to occur is to have an interface where the complex dielectric constants of the conductor and the surrounding material have opposite signs [34]. This condition is met for example by air-metal and glass-metal interfaces within the optical wavelength region.

From the Maxwell equations, one can derive the dispersion relation for SPs on a flat surface [38, p. 26]

$$k_{\mathrm{SP}} = k_0 \sqrt{\frac{\epsilon_d \epsilon_m}{\epsilon_d + \epsilon_m}}\,, \tag{3.16}$$

where k_{SP} is the wavenumber of the SP, k_0 the wavenumber in the surrounding medium and ϵ_d and ϵ_m the dielectric constants of the surrounding material and the

metal. For large values of k the SP frequency approaches the value

$$\omega_{\mathrm{SP}} = \frac{\omega_p}{(1+\epsilon_d)^{\frac{1}{2}}} \tag{3.17}$$

which is known as the *surface plasmon frequency* [38, p. 28].

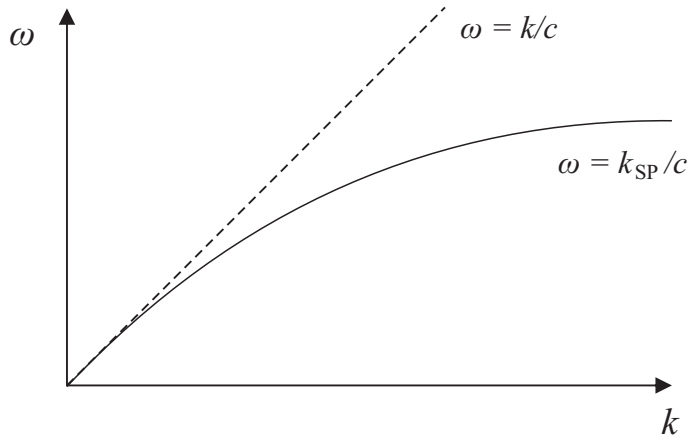

Figure 3.2: Dispersion relation of SPs (solid line) and light (dashed line).

The dispersion relation (Fig. 3.2) shows that the wavenumbers for light and SPs are different for all frequencies. This means that SPs cannot spontaneously decay into photons and are non-radiative. However, the dispersion relation can be changed by modifying the surface by for example, roughening it, which can give raise to photon-SP coupling. One method is fabricating a periodic surface structure which creates gaps into the dispersion relation [34]. This allows the wavenumbers to match at some frequencies which means that light and SPs can interact. This phenomenon is called a *surface plasmon resonance* and can be observed as a peak in the extinction spectrum of the material.

Like all electromagnetic radiation in conductive materials, SPs are damped while they propagate and can only travel a limited distance before they die out. This distance is known as *propagation length* δ_{SP} and can be written as [34]

$$\delta_{\mathrm{SP}} = \frac{c}{\omega}\left(\frac{\epsilon'_m + \epsilon_d}{\epsilon'_m \epsilon_d}\right)^{\frac{3}{2}} \frac{(\epsilon'_m)^2}{\epsilon''_m}, \tag{3.18}$$

where the dielectric constant of the metal has been separated into real and imaginary parts $\epsilon_m = \epsilon'_m + i\epsilon''_m$. The propagation length is wavelength dependent and varies with different metals. Silver and other noble metals have the longest propagation lengths in the 10-100 μm range. The propagation length of a material limits the possible dimensions of SP-based structures fabricated from it.

SP-light interaction can enhance the optical response of a material, such as SHG.

Because the properties of SPs can be tailored easily they have many applications in optical and photonic devices. Since the wavelengths of SPs are much smaller than visible light these devices can be built at a very small scale. Applications based on SPs include micro- and nano-optical devices [35], waveguides for use in telecommunication [36] and sensitive biosensors [37].

Localized Surface Plasmons

In the case of metallic particles with dimensions below the wavelength of light and the propagation length, the plasmons are called *localized surface plasmons* (LSP), or *localized particle plasmons*. LSPs oscillate within the entire volume of the particle and can give rise to strong resonances and near-field enhancement. They can also directly couple with light [38, p. 65]. The properties of LSPs are sensitive to particle size, shape and orientation with respect to each other and the polarization of incident light.

LSPs are linked to scattering and absorption of light by metallic nanoparticles. A quantitative theory of scattering and absorption by sub-wavelength particles, *Mie theory*, was developed by Gustav Mie in 1908 [39]. This approach leads to rigorous calculations involving electrodynamics and was not useful for practical purposes until the emergence of modern computers. Another limitation of Mie theory is that analytic solutions to the scattering problem are only possible for spherical and ellipsoidal particles.

The nanoparticles studied in this work are not ellipsoidal which means that their plasmonic properties must either be handled numerically or determined experimentally. Some general ideas can be derived from properties of ellipsoids but exact details are left to experimentation. An important type of particle concerning this work is a nanobar. Such particle has two primary resonances (Fig. 3.3) each coupling to a different polarization state of light. The resonance associated with the

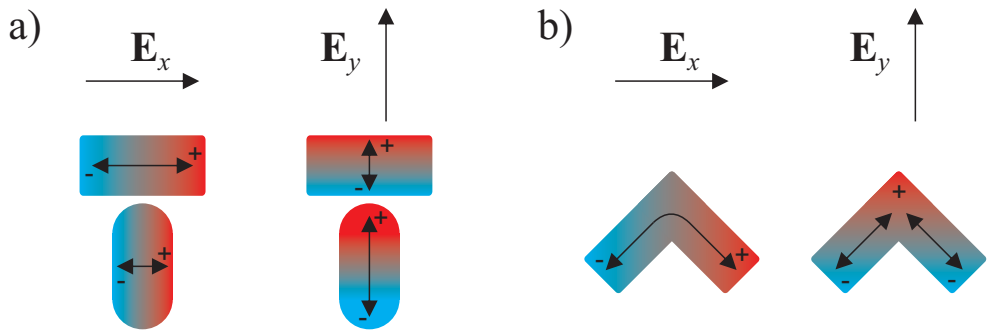

Figure 3.3: Plasmon resonances related to electric dipoles in two particle shapes: a) T-shape formed of two nanobars and b) L-shape

length of the bar has a longer wavelength than the resonance associated with the width. Generally the properties of resonances associated with rod-like particles depend on the ratio between the length and width of the particle. A long and thin bar has a large difference in resonant wavelengths while for a bar closer to circular shape they differ only little. Increases in particle size cause a redshift in both resonance wavelengths [24, p. 329]. Similar to bars, the L-shaped particle also has two primary plasmonic modes linked to different polarization states: one oscillating along the length of the entire particle and the other along each arm separately. The exact wavelengths and strengths of the resonances can be determined experimentally with spectroscopic measurements and theoretically calculated with numerical simulations, such as finite-difference-time-domain method (FDTD) [11] or boundary element method (BEM) [6].

Local Field Enhancement

Electric dipoles are induced in most materials when exposed to an electric field **E**. The induced dipoles are aligned with the external field which creates a polarization field **P** inside the material in the opposite direction compared to the external field. When the material polarization is superpositioned with the original electric field, the resulting field is weaker than the original field. This behavior is normal for dielectric materials.

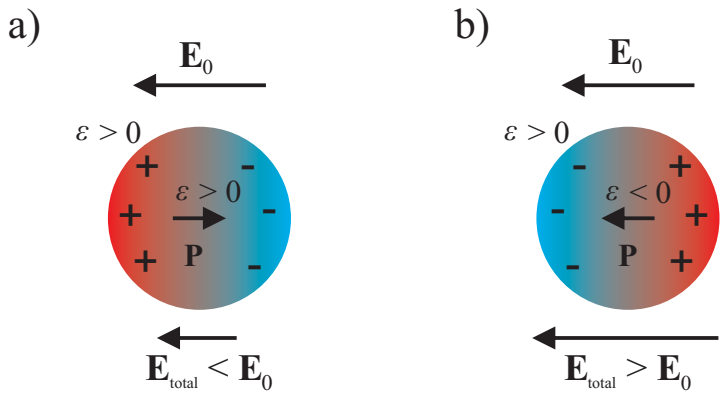

Figure 3.4: The local field inside a nanoparticle in a dielectric environment is a) weakened if the particle is dielectric or b) enhanced if the particle is plasmonic.

Plasmonic materials have an opposite effect when they are exposed to an external field. Because the real part of permittivity is negative the external field will induce dipoles in alignment with itself. This results in a material polarization in the same direction as the external field and the electric field is strengthened inside the medium, as illustrated in Figure 3.4.

Such *local field enhancement* is an important factor when considering the optical properties of metallic nanoparticles. Generally the field enhancement is not uniform and strong fields tend to form near the edges of particles, especially in any sharp features in the particle shape. Small gaps between particles can also exhibit strong local fields. These small areas of extreme field enhancement are referred to as *hot spots* [38, p. 159]. Theoretically local-field enhancement factors of up to $10^6 - 10^7$ have been predicted for ideal structures [18, 40]. Field enhancements up to order of magnitude 10^2 have been observed experimentally [41].

Local-field enhancement is a major factor in all phenomena that scale with electric field strength. This makes materials with strong local-field enhancement desirable in nonlinear optics since nonlinear effects are related to a higher power of the electric field.

3.4 Second-harmonic Generation from Metal Nanoparticles

We concluded previously that in order to observe SHG the medium must not be centrosymmetric. If we ignore their thickness and consider them as planar shapes, the T- and L-particles both belong to symmetry point group C_{1v}. This means they have a single mirror axis and no other symmetry operations (Fig. 3.5). They are not centrosymmetric and so can produce a SHG signal.

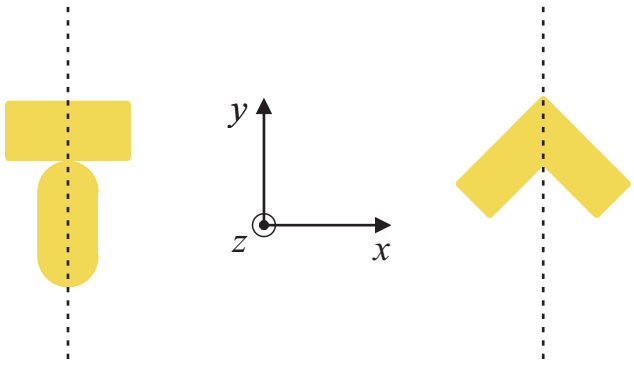

Figure 3.5: The only symmetry operation of the particles studied in this work is reflection with respect to yz-plane.

As stated before, not all components of the susceptibility tensor are independent. Some can be zero due to symmetry, which are called *forbidden components* while some components can be forced to be equal and non-independent. The non-zero components are called *allowed components*. To find the allowed components of the susceptibility tensor we must consider the coordinate transformations of the tensor. For a third-rank tensor a coordinate transformation is defined with the

equation [42, p. 133]

$$B'_{ijk} = \sum_{lmn} \frac{\partial i}{\partial l}\frac{\partial j}{\partial m}\frac{\partial k}{\partial n} B_{lmn}\,, \tag{3.19}$$

which describes a coordinate transformation from coordinate system (l, m, n) to coordinate system (i, j, k). In addition, if the coordinate transformation is a symmetry operation the tensor must remain unchanged. In the case of the operation in Figure 3.5 for our T-shape the coordinate transformations are as follows

$$x' = -x \qquad y' = y \qquad z' = z\,. \tag{3.20}$$

Letters x', y' and z' refer to the coordinates of the mirror image while the plain letters are the original. With these coordinates we can calculate the partial derivatives in the tensor coordinate transformation formula

$$\begin{array}{lll} \dfrac{\partial x'}{\partial x} = -1 & \dfrac{\partial y'}{\partial x} = 0 & \dfrac{\partial z'}{\partial x} = 0 \\ \dfrac{\partial x'}{\partial y} = 0 & \dfrac{\partial y'}{\partial y} = 1 & \dfrac{\partial z'}{\partial y} = 0 \\ \dfrac{\partial x'}{\partial z} = 0 & \dfrac{\partial y'}{\partial z} = 0 & \dfrac{\partial z'}{\partial z} = 1\,. \end{array} \tag{3.21}$$

We can now transform the susceptibility tensor to the new coordinates. Each component of the tensor must be transformed separately. For example, calculating the component $\chi^{(2)}_{x'x'x'}$ yields

$$\chi^{(2)}_{x'x'x'} = \sum_{lmn} \frac{\partial x'}{\partial l}\frac{\partial x'}{\partial m}\frac{\partial x'}{\partial n}\chi^{(2)}_{lmn}\,. \tag{3.22}$$

When we substitute the partial derivatives in (3.21) we can see that all but one term in the sum becomes zero. The leftover term we can calculate to be

$$\chi^{(2)}_{x'x'x'} = \frac{\partial x'}{\partial x}\frac{\partial x'}{\partial x}\frac{\partial x'}{\partial x}\chi^{(2)}_{xxx} = (-1)(-1)(-1)\chi^{(2)}_{xxx} = -\chi^{(2)}_{xxx}\,, \tag{3.23}$$

which means that $\chi^{(2)}_{xxx}$ must be zero because the susceptibility tensor cannot change after a symmetry operation. Thus the SHG component $\chi^{(2)}_{xxx}$ is forbidden.

If we go through all tensor components, we see that components χ_{ijk} with odd number of x-indices transform into $-\chi_{ijk}$ and thus must be zero, and components with even number of x-indices transform into χ_{ijk}. From this we can conclude a rule that all SHG components with even number of x-indices are allowed, and all components with an odd number of x are forbidden.

We can also apply intrinsic permutation symmetry equation (3.9) to the allowed components. This allows us to switch the two input indices and the susceptibility

must stay the same. This symmetry forces some components to be equal to each other. Finally, because we will later only consider the case where light is at normal incidence, we can ignore all components including the coordinate z. With these considerations the only nonzero tensor components we need to take into account are the allowed components

$$\chi^{(2)}_{yyy}, \chi^{(2)}_{yxx} \text{ and } \chi^{(2)}_{xxy} = \chi^{(2)}_{xyx} \,. \tag{3.24}$$

Consequently, the forbidden components are

$$\chi^{(2)}_{xxx} = \chi^{(2)}_{xyy} = \chi^{(2)}_{yxy} = \chi^{(2)}_{yyx} = 0 \,. \tag{3.25}$$

Nonlinear Response Tensor

The nonlinear response from an array of nanoparticles is sensitive to various effects at the nanoscale. Especially when a plasmon resonance is excited the local field can have strong local variations. Modeling these effects in the nonlinear response theoretically or computationally is challenging and typically analytical solutions do not exist. Instead, the nonlinear response tensor (NRT) model [43] was used to make a theoretical fit to the data collected from nonlinear measurements. The NRT approach treats the sample as an effective medium and only the macroscopic response of the material is considered instead of individual particles [44]. Localized nanoscale effects are not taken into account separately and are part of the macroscopic susceptibily.

The NRT model can be written as

$$E_i(2\omega) = \sum_{j,k} A_{ijk} E_j(\omega) E_k(\omega) \,, \tag{3.26}$$

where A_{ijk} is the nonlinear response tensor. If we can assume that the measured output field is caused entirely by SHG from the sample, then the components of NRT are directly related to the values of the nonlinear susceptibility tensor components in equation (3.8). In the experimental setup this is ensured by the use of filters to block excess signals. Because we do not handle exact numerical values of either in this work, it is enough to know that the ratios between the susceptibility tensor components are equal to the ratios of the NRT tensor components. This also means that we need not know the exact relations between fields, photon counts and tensor components.

The photon count measured in the experiment is proportional to the intensity which is in turn related to the square of the electric field associated with light. Thus when fitting into the data expressed in photon number N we instead use the square

of the absolute value

$$N_i(2\omega) \propto |\sum_{j,k} A_{ijk} E_j(\omega) E_k(\omega)|^2 \,. \tag{3.27}$$

When we take into account the simplifications in our experiments we can modify the expression further. In the experiments we always use light with normal incidence and only need to consider polarization components x and y. For each polarization the output can be written as

$$N_x \propto |A_{xxx}\mathbf{E}_x^2 + A_{xyy}\mathbf{E}_y^2 + 2A_{xxy}\mathbf{E}_x\mathbf{E}_y|^2 \tag{3.28}$$
$$N_y \propto |A_{yxx}\mathbf{E}_x^2 + A_{yyy}\mathbf{E}_y^2 + 2A_{yxy}\mathbf{E}_x\mathbf{E}_y|^2 \,. \tag{3.29}$$

The last terms have a factor of 2 because the terms are sums of two identical components ixy and iyx, a result of intrinsic symmetry (3.9). A further simplification can be made by removing the forbidden SHG components (3.25) from the fitting model and only include allowed components (3.24)

$$N_x \propto |2A_{xxy}\mathbf{E}_x\mathbf{E}_y|^2 \tag{3.30}$$
$$N_y \propto |A_{yxx}\mathbf{E}_x^2 + A_{yyy}\mathbf{E}_y^2|^2 \,. \tag{3.31}$$

For high-quality samples this is a fair assumption. The NRT components are complex valued in the general case but in this work we have assumed them to be real. In addition to the NRT components, a scaling parameter C_i was included to match the fit to the numerical values obtained in measurements and the final model is described by the relations

$$N_x = C_x|2A_{xxy}\mathbf{E}_x\mathbf{E}_y|^2 \tag{3.32}$$
$$N_y = C_y|A_{yxx}\mathbf{E}_x^2 + A_{yyy}\mathbf{E}_y^2|^2 \,. \tag{3.33}$$

4. RESEARCH METHODS

"No amount of experimentation can ever prove me right; a single experiment can prove me wrong."

- Albert Einstein

4.1 Sample Fabrication

The samples studied in this work are gold nanoparticles on a silica substrate arranged in a square array. The samples were fabricated at the University of Eastern Finland using electron beam lithography, vacuum deposition and mask liftoff.

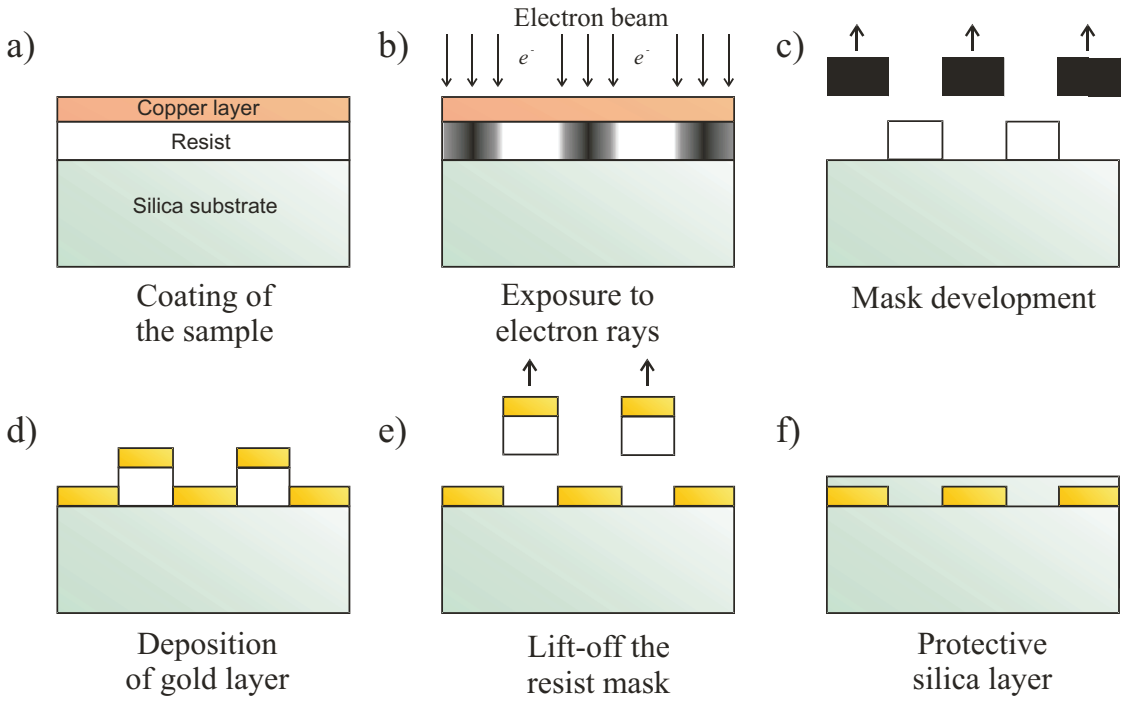

Figure 4.1: Steps of fabrication process (electron beam litography and litfoff).

Electron beam lithography is a method which allows preparation of samples with high nanoscopic resolution [19]. The fabrication process comprises of six steps presented in figure 4.1. First the sample is coated with a layer of resist material

(polymethyl-metacrylate, PMMA) which is sensitive to electron beams. A thin layer of copper is deposited on top of the PMMA layer to prevent the sample from being charged during the electron beam exposure. The resist layer is exposed to an electron beam to imprint the nanoparticle pattern. A pattern resolution of the order of a few nm can be achieved with this method [45, 46]. After exposure the resist mask is developed with a solvent, which, depending on the material and solvent, removes either the exposed or non-exposed areas of the resist layer. The sample is then coated with a thin adhesive contact layer and a 20 nm layer of gold. The remaining resist mask is lifted off using another solvent, leaving behind a silica substrate coated with a gold nanopattern. To protect the sample from chemical and physical wear it is coated with a protective layer of evaporated silica.

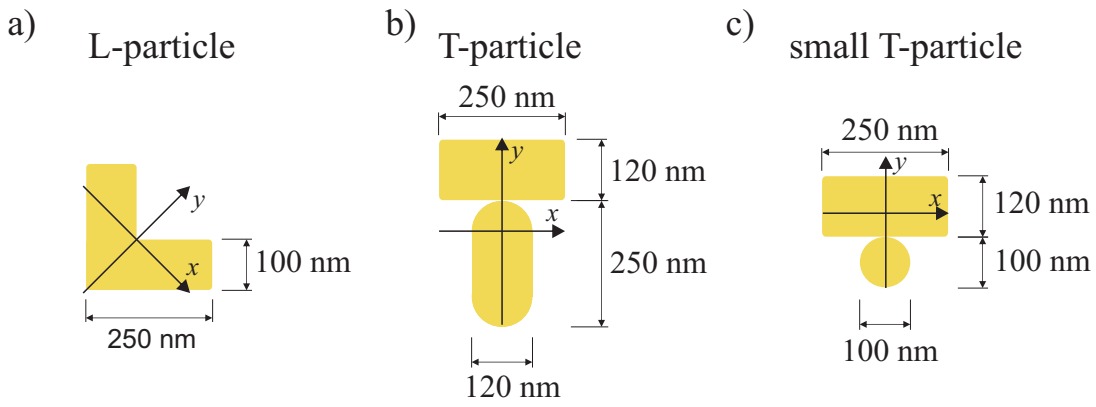

Figure 4.2: Dimensions of nanoparticles and coordinate systems used for the samples.

The studied samples are square arrays of T- or L-shaped nanoparticles with a grating period of 500 nm. The array of L-shaped nanoparticles (sample L) is our reference sample (Fig. 4.2a). Such samples have been previously studied with the results pointing out high quality [20, 47]. The T-shaped nanoparticles are composed of two elements: a horizontal bar and either a vertical bar (Fig. 4.2b) or a dot (Fig. 4.2c). Furthermore there are two variations of the particles: samples A and C (upper row in Fig. 4.3b) are designed in such a way that the two components are touching at one point (0 nm gap) while in samples B and D they are overlapping by 10 nm (lower row in Fig. 4.3b). There were also samples fabricated with gaps between the components but those yielded uninteresting results and are thus not discussed in this work. In order to double check sample quality, we studied two separate sets of samples named test and final samples. Both are identical in design and the only difference is that the test sample lacks the final protective silica layer (step f in Fig. 4.1).

The coordinate system used to describe light polarization relative to the orien-

tation of the samples is also presented in Figure 4.2. For all particles the y-axis is along the symmetry axis of the nanoparticle and the x-axis is perpendicular to it (Fig. 4.2).

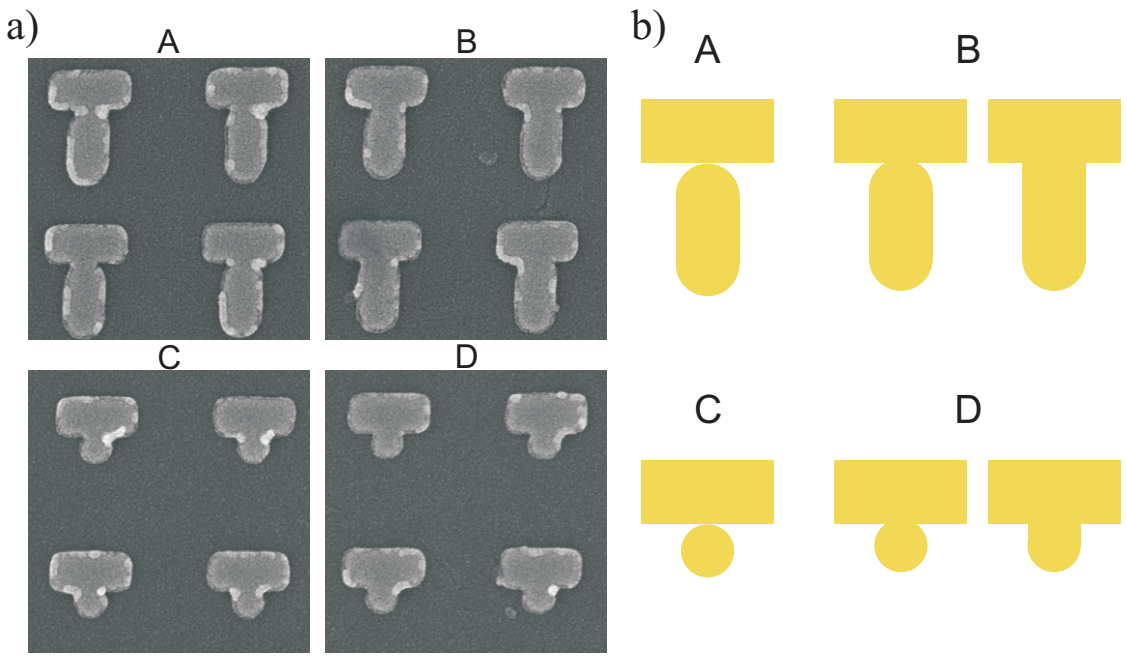

Figure 4.3: a) SEM-images of the studied samples. b) Designs of the final samples.

The SEM images, presented in Figure 4.3a, show that although quality of nanoparticles is good, the sharp features of the samples are supressed. Particularly this is visible in the case of samples B and D. Partially this is due to the fact that in order to take SEM pictures a conductive layer is needed. For that reason particles were coverd by a layer of copper which tends to aggregates in gaps. On the other hand, the sharp features are always the most difficult to fabricate. Nevertheless, in order to make modeling close to reality, we'll use a design without sharp features between the two components forming the T-shaped particles. Such "mushroom"-shape is presented in Figure 4.3b on the rightmost column.

4.2 Linear Measurements

The linear optical properties of the samples were studied by measuring their extinction using the experimental setup shown in Figure 4.4. All samples were measured at normal incidence and the spectra include both absorption and scattering because it is not possible to separate them with our setup.

As a source, a broadband halogen light was used which was delivered into the setup with an optical fiber. The light was collimated by a micrscope objective in

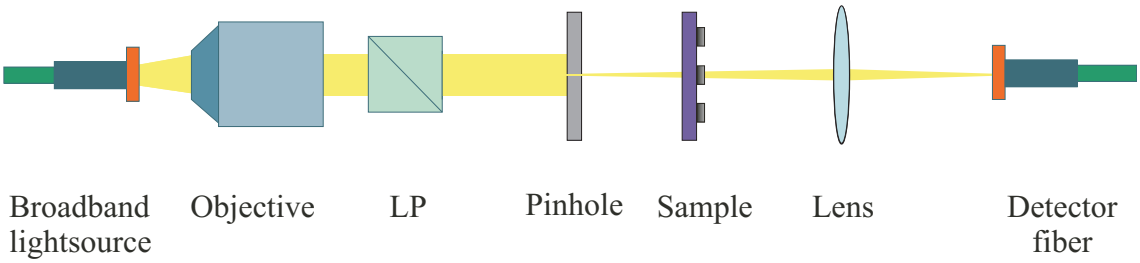

Figure 4.4: Spectrometer setup for extinction spectra measurements.

order to overcome its strong divergence. Due to the fact that our particles are strongly dicchroic, we measured the extinction spectra for polarizations x and y. A linear polarizer was used to control the polarization of the input light. Since the collimated beam was much larger than the sample areas (1 mm x 1 mm squares), a pinhole was used to limit the area of the beam and only illuminate one sample area at a time. After the sample the beam was focused to another fiber which leads it to a spectrometer to be analyzed. The spectra were measured for a range of 400 - 1700 nm and in order to cover the full range two spectrometers were used (Avantes AvaSpec-2048, Avantes NIR256)

4.3 Nonlinear Measurements

SHG from the samples was measured using the setup shown in Figure 4.5. A Nd:glass femtosecond laser (wavelength 1060 nm, pulse length 200 fs, repetition rate 82 MHz, average power 150 mW) was used as a light source. The laser beam was polarized with a linear polarizer (LP) and led through a motorized half-wave plate (HWP) in order to continuously rotate it during the experiment. In total the input polarization was rotated 180° during one measurement, which equals 360° rotation in polarization angle. The step size between measurement points was 2°. Another polarizer, placed before the photomultiplier tube, was controlling the polarization of the SHG signal. The measurements were performed at two linear polarization states corresponding to the main axes of the nanoparticles.

The filters were used to select the desired wavelength of light. A visible block filter was placed before the sample to block all SHG light generated by the components. An IR-block filter was placed after the sample in order to trasmit SHG radiation only. The beam was focused to one sample area at a time with a lens. A lens with large focal length was used so that the beam profile would be close to a plane wave

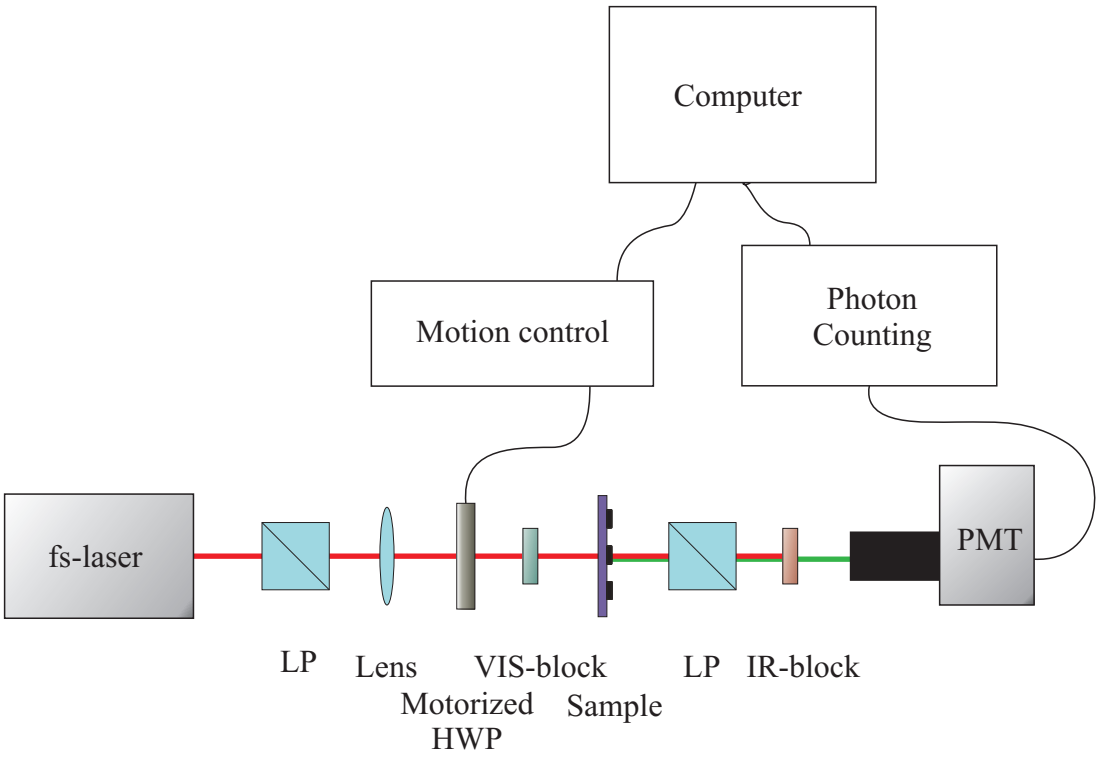

Figure 4.5: SHG experimental setup.

and normal incidence can be assumed in addressing the results. Also, too tight focusing raises the local irradiance high which could damage the nanoparticles.

The SHG radiation was detected by a photomultiplier tube (PMT) connected to a photon-counting unit. A narrow pass filter was placed on the PMT to block background noise. To further limit noise, the entire setup was placed inside a black cardboard box. With these precautions, background signal could be reduced to a few photons per second. Light was collected for 5 seconds in each measurement point.

4.4 Numerical Methods

To support the experiments, numerical simulations were run and compared to the results. Two methods were used in the calculations: finite-difference-time-domain (FDTD) and boundary element method (BEM) [6]. Both are well known methods and have been widely used in many fields of physics and engineering for decades [48–50]. Combined with modern computing power they are an effective tool for studying electrodynamics of nanostructures. The mathematics used in the methods are way beyond the scope of this work so the general ideas involved in the methods are discussed only briefly. The programs used in the simulations were written by Jouni Mäkitalo, a colleague in our lab.

Finite-difference Time-domain

In FDTD the continuous electrodynamics problem is approximated with discrete cells. This transforms the differential Maxwell equations into finite difference equations which can be solved using discrete time steps, hence the name of the method. At each time step the electric and magnetic fields are calculated in each cell and the process is continued until a steady-state solution is reached [51].

The FDTD program allows theoretical calculation of extinction spectra, local field distributions and field enhancements. The sample is inputted as a bitmap and the resolution can be arbitrarily precise. However, due to the amount of calculations required, setting the resolution too high will make the timescale of calculation too long for practical use. A disadvantage in pixelating the sample is that small details such as the gap areas in samples A and C are deformed. However, the gap is hardly ideal on the actual samples either (Fig. 4.3a) so we deemed this not to be a problem.

Boundary Element Method

BEM involves reformulating the partial differential equations governing the system into discrete boundary integral equations mathematically equal to the original problem. These integral equations are fitted to match boundary conditions which then allows numerical calculation of the solution at any point in the domain [52].

Conceptually this means that only the boundaries of the domain need to be discretized for solving the problem, as opposed to the entire domain in FDTD. For example with the nanoparticles studied in this work, only the surfaces of particles are involved in the computation. The surfaces are represented with a mesh grid made out of triangles. The grid does not need to be uniform over the entire domain. For example the triangles can be big over large flat surfaces and smaller when the surface has a higher curvature [52].

Generally BEM can lead to more effective computations compared to other numerical methods wherever it is applicable since there are fewer pixels involved in the calculation. However, the method is not as universal as for example FDTD. For example, BEM is is not suitable for simulating the samples A and C in this work, since the infinitely small gap area causes the equations involved in the method to become badly behaved. Since we still wanted to make calculations using BEM for all samples the particles were considered to overlap by a small margin for these calculations. This allows BEM to work and is not far from the fabricated particles seen in the SEM images (Fig. 4.3).

5. RESULTS

"The great tragedy of Science - the slaying of a beautiful hypothesis by an ugly fact."
- Thomas H. Huxley

5.1 Extinction Spectra

The extinction spectra of all the samples were measured using the setup described in Section 4.2, using both x- and y-polarized light and they are presented in the form of optical density (Eq. 2.27) as a function of wavelength. The spectra for the reference sample are presented in Figure 5.1 and for samples A-D in Figure 5.2. The dotted vertical red line shown in the graphs represents the wavelength of the laser used in the nonlinear experiments.

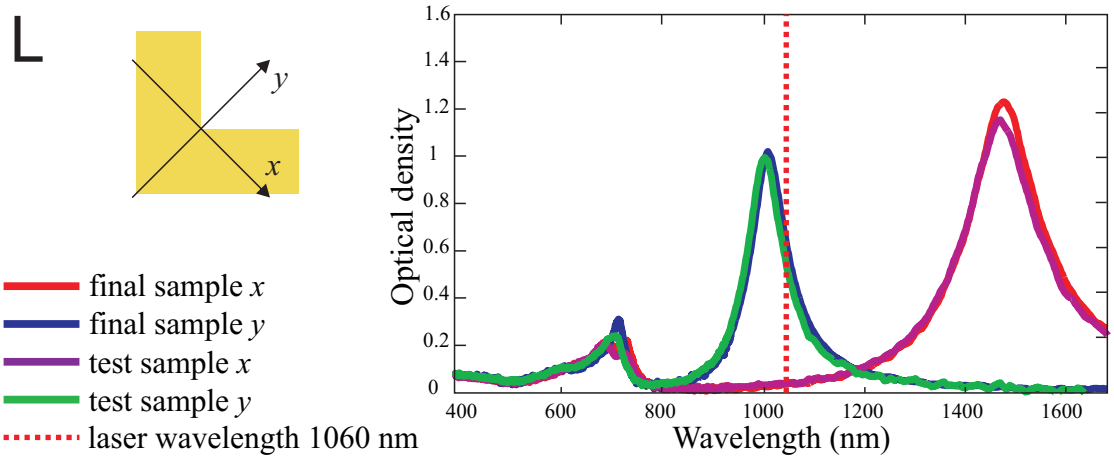

Figure 5.1: Extinction spectra of the L sample.

The L-shape has strongly dichroic fundamental resonances, each associated with a different polarization state of light. The properties of these fundamental resonances are highly dependent on the dimensions of the L-particle. Previous studies have shown that the resonances can be tuned over a large spectral range by varying the properties of individual particles [11], as well as the entire structure [47]. For the samples measured in this work, the y-resonance is located near the laser wavelength, at around 1000 nm, as was intended in sample design. The x-resonance is in the

infrared, at around 1500 nm and thus is not resonant with the laser. The resonances at shorter wavelengths around 700 nm are associated with the width of the arms of the L-particle. There are no significant differences in the spectra between samples. These results are similar to the ones observed earlier on a similar sample [47] which suggests that our samples have high quality, equal to previously studied L-shaped nanoparticles.

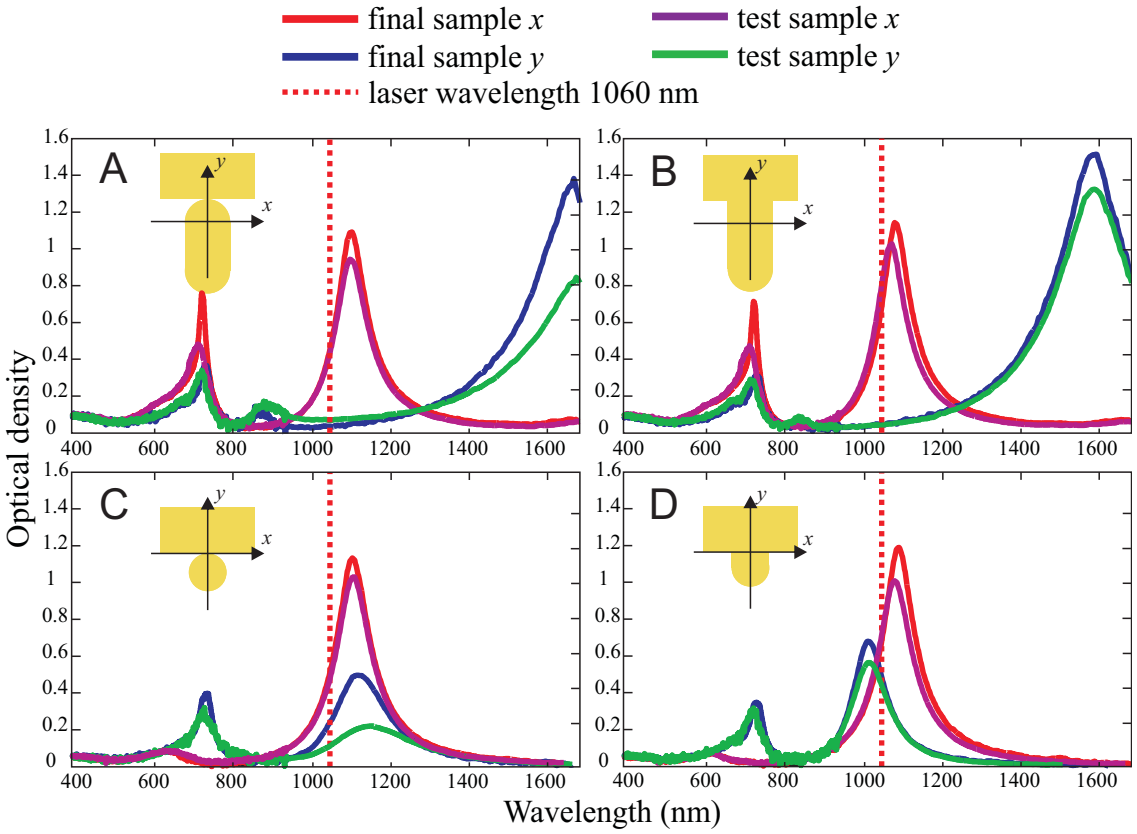

Figure 5.2: Extinction spectra of the T-shaped samples.

The spectra of samples A-D (Fig. 5.2) are similarly dichroic with each fundamental resonance associated with a different polarization state. For all samples, the x-resonance is associated with the length of the top (horizontal) bar of the T-shape and is near the laser wavelength, at about 1100 nm, for all samples. The x-resonance of the samples with connected particles B and D lies at a slightly shorter wavelength compared to A and C. This suggests that the more distinct gap area in samples A and C influences the resonances and causes the bars to act more like separated particles.

For y-polarization the wavelengths vary more between the samples. For samples A and B the y-resonance lies far in the infrared (1600-1700 nm), away from the laser wavelength, while samples C and D have a resonance at the laser wavelength. This is expected behavior since the particle height is much larger in the case of

the T-particles in samples A and B. As with x-resonances, the y-resonances are also slightly blueshifted for samples B and D when compared to A and C. This is credited to the overlapping of the particles in samples B and D. Due to overlapping particles the nanostructure is 10 nm shorter than in the non-overlapping case, which changes the resonant wavelength of the particles.

As with L-particles, all the samples have resonances between 700-800 nm. These are related to bar widths in the particles which were designed to have a width associated resonance at 760 nm. This spectral region is also influenced by higher-order modes, as evident from the asymmetry of the peak. This irregular shape could arise from multiple resonances near each other. Also in the spectra of samples A and B there are some weak resonance peaks at around 850 nm. We are not certain about the nature of these resonances. They appear to be related to the gap area or the lower bar of the T-shape. They could be modes oscillating within the edges of the lower bar due to the fact that the resonances are much weaker in sample B, where the gap area is less distinct. However, for all samples, these shorter wavelength resonances are not significant considering the rest of this work because they are not resonant with either our laser or SHG frequencies and thus do not influence the nonlinear effects discussed further on.

Table 5.1: Wavelengths, bandwidths and strengths of main resonance peaks. Resonances that match with the laser wavelength are highlighted in yellow.

x-polarization

	λ (nm)		FWHW (nm)		Optical density	
	final	test	final	test	final	test
L	1494	1487	180	188	1.231	1.154
A	1117	1112	97	107	1.091	0.943
B	1093	1086	97	100	1.143	1.026
C	1118	1123	110	118	1.134	1.031
D	1105	1093	104	114	1.190	1.008

y-polarization

	λ (nm)		FWHW (nm)		Optical density	
	final	test	final	test	final	test
L	1023	1017	92	90	1.019	0.994
A	1686	1692	242	284	1.382	0.846
B	1611	1605	244	120	1.515	1.324
C	1130	1168	158	244	0.495	0.222
D	1023	1029	100	115	0.680	0.564

With samples A-D there are more significant differences between the spectra than with L samples. The differences are still small, with the test sample having slightly weaker extinction within the resonance peaks. The two exceptions are the spectra

of samples A and C for y-polarization where the fundamental resonance of the test sample is only half as strong as that of the final sample. Of these, only sample C has a difference near the laser wavelength. This difference could be caused by lack of the final protective layer, quality in sample fabrication or damage in the sample.

The results from the linear measurements including the exact wavelengths of each resonance, the full width at half maximum (FWHM) of each peak and the strength of the resonance expressed with optical density are collected in Table 5.1. The widths of the resonance peaks are linked with the homogeneity of the particles in the sample area and are good indicators of quality of the samples. Comparing the FWHM of the L-particles to previous results [1, p. 52], we can see that the samples researched in this work are of equal quality to the best samples studied earlier.

Comparison to Numerical Models

Numerical simulations were ran to make comparisons with the measured extinction spectra. BEM was used to calculate theoretical extinction spectra for the samples over the visible range. In the simulation, broadband light with a Gaussian line shape was used as a light source in order to cover the entire spectral range used in the experiments. The program uses a local model with one particle, and the electric fields are set to match at opposite boundaries to introduce an effective periodic structure. To avoid problems involving infinitely sharp features, the samples A and C were approximated with the particles overlapping by 2 nm instead of touching at one point. For samples B and D two different simulations were done: one using particles with a rounded gap area and the other with particles without any gap features (see Fig. 4.3b). Also in the calculation the chromium layer present in the samples was not included due to the challenges associated.

The calculated BEM spectra are presented in Figure 5.3 along with the measured spectra for the final sample. Generally the shapes of the calculated spectra agree with the measurements and the main differences are in resonance wavelengths. All the main resonances are redshifted compared to the measurements. Whether this is caused by the lack of the chrome layer in the simulation or another shortcoming is unknown. Overall the simulated results resemble the measured results better with samples B and D than with A and C, which were known to be computationally challenging structures.

The most significant observation about the numerical results is that the measured spectra for samples B and D match better with the calculations done using the particle model without any gap area. This would suggest that this particle shape is closer to the actual fabricated particles, as already speculated with the SEM pictures. Especially the y-polarized "no gap" -simulation for sample B is almost a perfect match to the measured data.

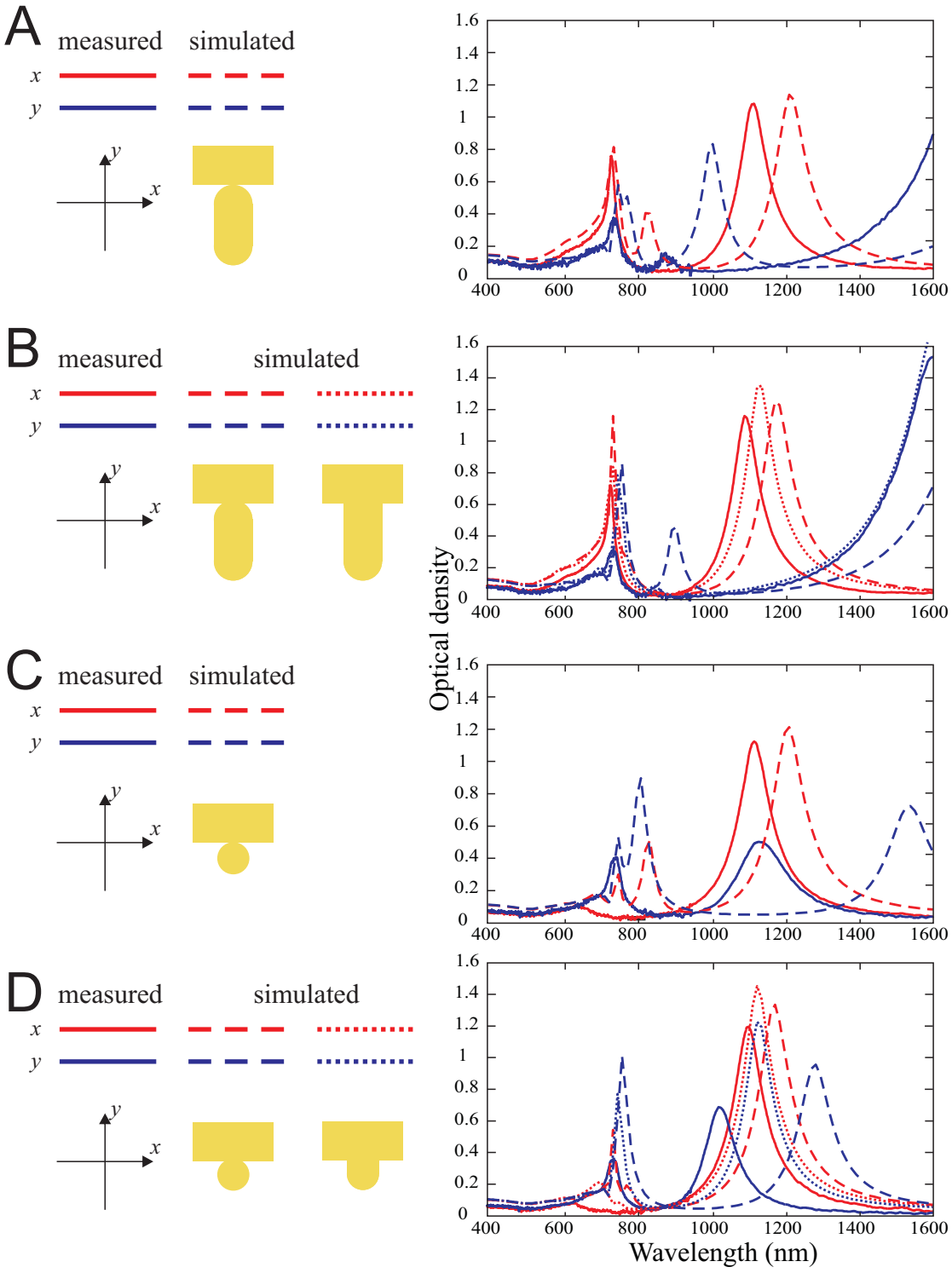

Figure 5.3: Comparison of experimental and calculated, using BEM, extinction spectra of studied samples.

Also, the calculations show a resonance at around 850 nm similar to some of the measurements. The calculations fortify the previous supposition that this resonance is related to the gap features since this resonance is missing from the calculated spectra for the "no gap" -models for samples B and D. This resonance is especially strong in the calculations for x-polarized spectrum of sample A where it is almost as strong as the main resonance for y-polarization. The explanation for why this resonance is not as strong in the measurements is likely the inhomogeneity of the gap areas in the samples which broadens and weakens the peak. The sharpness of the resonance at 750 nm suggests that it could be influenced by a lattice mode arising from diffractive coupling within the structure. The wavelength matches that of the grating period 500 nm multiplied by the refractive index of glass ($\approx$ 1,5). In the calculated spectrum for sample C we see a split resonance which suggests that the resonances at 700-800 nm are all influenced by the lattice modes, higher-order resonances and the resonance associated with the bar width.

5.2 Second-harmonic Generation

Nonlinear measurements were performed with the setup described in Section 4.3. The measured results are expressed in terms of photon counts as a function of the polarization angle of incident light. A fit was made for each measured dataset with the NRT model described in Section 3.3 (Eq. 3.32). The fitting was done with MATLAB using the *nlinfit*-function.

L-Shaped Particles

The measured SHG signals for the L-particle samples are presented in Figure 5.4. In all further graphs the starting angle 0° represents y-polarized light and all angles associated with the susceptibility tensor components are marked with vertical dashed lines. The NRT fit matches the measured data very well for y-polarized output. For x-output the model doesn't fit so well because the model output it forced to zero at angles corresponding to pure forbidden components A_{xyy} and A_{xxx}. This is a common problem when the overall signal level is very low.

The final L sample generates a high SHG signal of about 2500 photons when both input and output signals are y-polarized. y-output with x-input yields a much weaker signal of about 300 photons. x-polarized output is very weak for all input polarizations with about 150 photons at maximum. The test sample has similar behavior with slightly lower photon counts overall. This means that the tensor component A_{yyy} is dominant for this type of sample.

This behavior is credited to the extinction spectra of the L-sample (Fig. 5.1). The sample has a plasmon resonance at the laser wavelength for y-polarized light

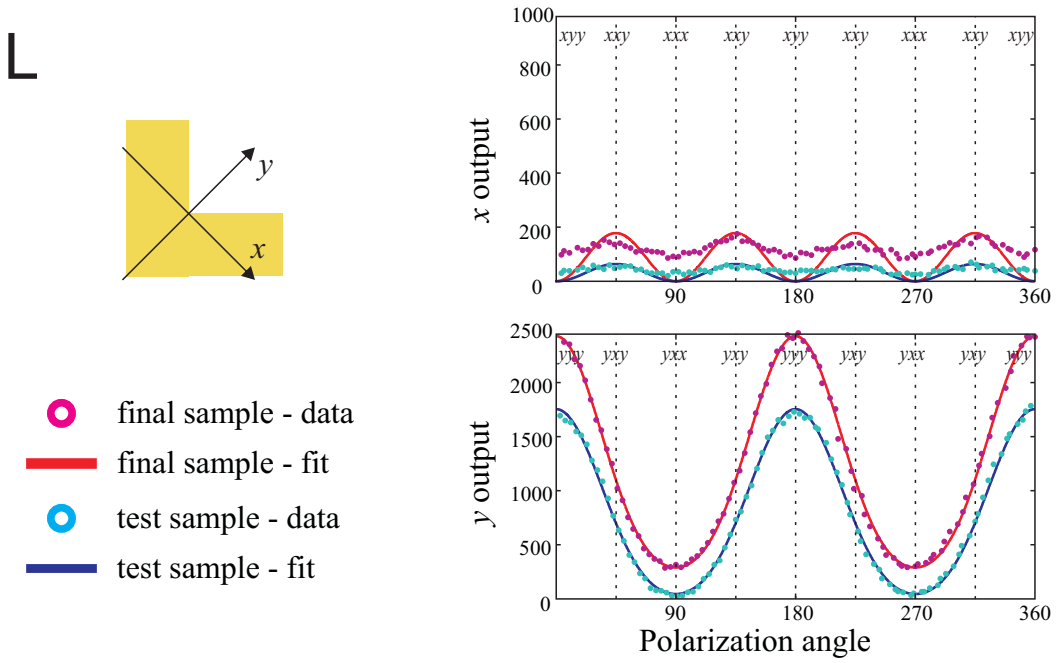

Figure 5.4: SHG counts for L samples.

while x-polarized light is non-resonant at the laser wavelength. The combination of allowed polarization component and a resonance at the input polarization yields a high SHG signal. The allowed non-resonant components (A_{yxx} and A_{xxy}) have weak signals and the forbidden components (A_{xyy} and A_{xxx}) are even weaker. The SHG signals from the reference sample thus follows the symmetry rules of SHG. These results match those that have been observed earlier with the same kind of L-particles [20, 44, 53]. With these results we can state that the quality of the samples is very good.

T-shaped Particles

SHG photon counts from the measurements on samples A-D are presented in Figure 5.5. As with the previous graphs for L samples, the polarization angle 0° equals to y-polarization and the signal levels associated with the susceptibility tensor components are marked with dashed lines.

For the output polarization x all graphs have a similar form but with different strength of amplitude. The allowed component A_{xxy} yields a high signal and the forbidden components A_{xxx} and A_{xyy} have very low signals. The signal levels of the final sample are at about 2000 photon counts for sample A and 1500 counts for sample, B which is a bit lower than the signals measured from the L reference sample. The SHG signals from samples C and D are about twice as strong reaching almost 5000 counts for the allowed components.

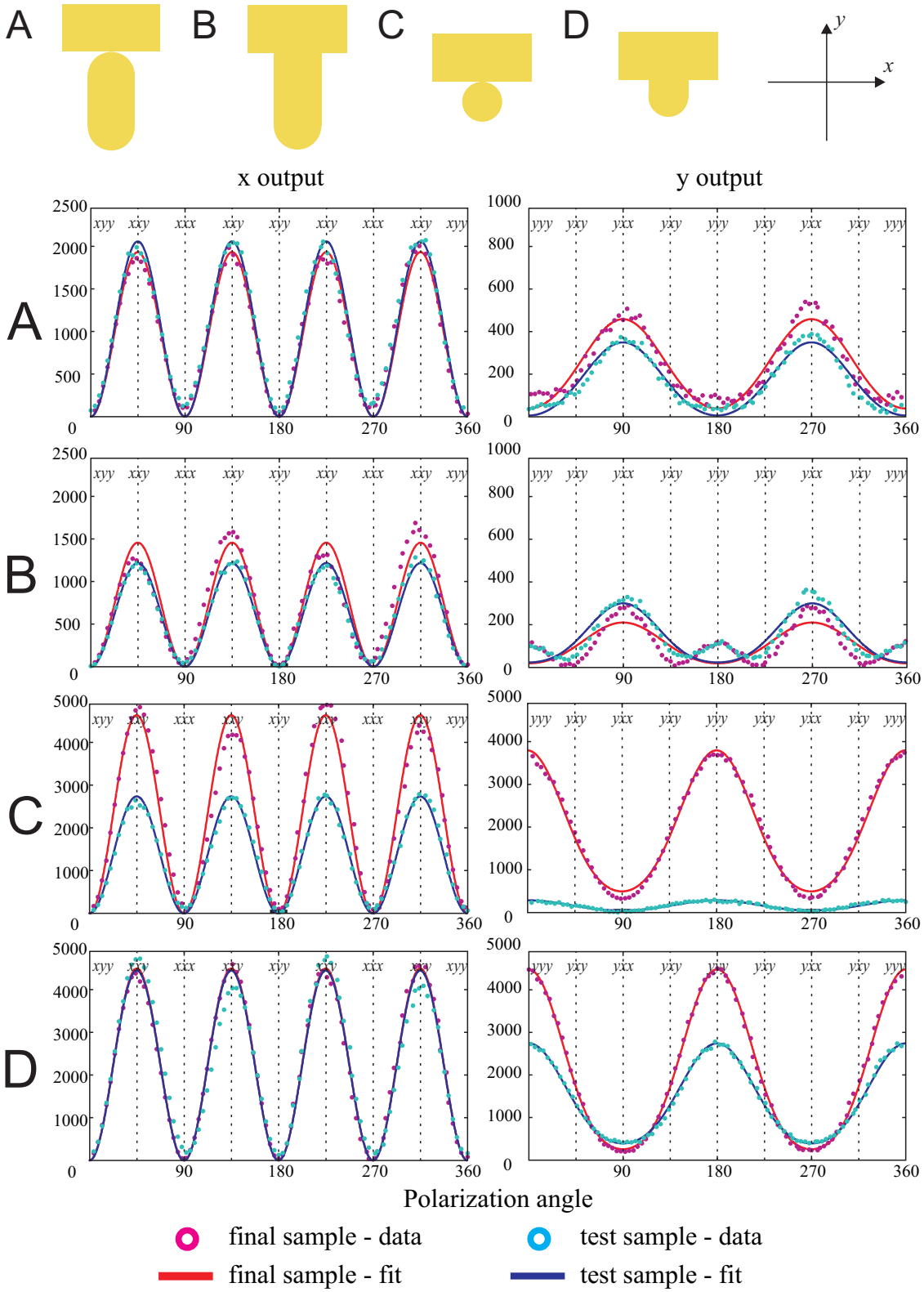

Figure 5.5: SHG counts as a function of input polarization angle for samples A-D. Zero angle equals y-polarized light.

The theoretical fit is a better match to the data than with the L samples, mainly because the signal levels are a lot higher. For samples B and C the fit gets skewed due to some variations in the measured signals between input angles $\pm 45°$ although both angles are associated with the same SHG component A_{xxy}/A_{xyx}. This is most likely due to a minor misalignment of the sample during the measurement or the sample itself could be defective. The latter explanation is supported because neat signals were measured from other samples with identical polarization setup and T-dimer samples with slanted vertical bars have been observed before [54]. A defect like this breaks the symmetry of the sample and can cause the two input polarization states to have different output signals. Since the most important issue are the orders of magnitude of the signals and not the precise photon counts we decided to use the measured data as is.

The stronger signal from samples C and D is explained through the resonances of the samples. Because the allowed component contains both polarization components the signal is amplified when either one is resonant. All the samples have a resonance at the input wavelength for x-polarization. Samples A and B are non-resonant with y-polarized light but when the vertical bar is exchanged into a dot in samples C and D, the resonance associated with y-polarized light is moved to a shorter wavelength and these samples are resonant at the input wavelength (figure 5.2). This means that both input photons can excite a plasmon resonance which results in a stronger second-harmonic signal.

The data for y-polarized output results in a relatively weak signal from samples A and B. The strongest signal is measured from component A_{yxx}, with photon counts of 600 (sample A) and 400 (sample B). This result is as expected since for these samples the component is allowed and resonant with the input field. Still, one would predict sample B to yield a stronger signal for this component since the resonance peak is closer to laser wavelength on that sample compared to A (table 5.1). This was the case with x-output as well which suggests that a gap area with narrow features enhances the SHG signal more than having a closer resonance with the laser. SHG signals from component A_{yyy} are weak for both samples A and B, as expected for allowed but non-resonant components. This component is clearly visible as a peak for sample B and barely distinguishable for sample A. However, the fitting model fails with these samples and for some reason can't take into account the peak at component A_{yyy} for sample B. The fit for sample A is also not totally accurate but the difference is not as striking as with sample B.

For y-polarized output from samples C and D we get strong signal of about 4000 counts. The NRT model fits the data very well, except for a slight difference in signal strength at component A_{yxx} for sample C. The strongest signal is measured for component A_{yyy} which is both allowed and resonant. However, component A_{yxx}

is also allowed and resonant for these samples but produces a SHG an order of magnitude weaker. This result is against the theoretical predictions about allowed components and plasmon resonances. For layout D the test sample produces a signal about a third weaker than the final sample which is justified by the slightly weaker resonances on that sample. Sample C on the other hand has a huge difference between the signal levels on final and test samples. While the final sample has a strong signal of 3600 photons, the signal from the test sample only measures about 400 counts. As previously with x-polarized output, this is explained by the much weaker y-resonance on the test sample. Because the component A_{yyy} is only associated with y-polarized light, the effect of the weaker resonance is amplified and the relative difference between signal levels is larger.

Table 5.2: SHG photon counts from measured data and fitted models for allowed SHG-components.

Final Sample

	xxy		yyy		yxx		Resonances
	data	fit	data	fit	data	fit	
L	150	170	2420	2420	290	290	y
A	1970	1920	280	230	600	560	x
B	1570	1450	160	70	320	250	x
C	4800	4600	3670	3780	320	500	x, y
D	4530	4470	4460	4460	210	260	x, y

Test Sample

	xxy		yyy		yxx		Resonances
	data	fit	data	fit	data	fit	
L	60	60	1800	1800	240	240	y
A	2050	2050	140	100	440	410	x
B	1210	1210	110	20	350	300	x
C	2720	2720	410	430	170	200	x, y
D	4680	4420	2730	2730	410	390	x, y

Both input photons resonant
One input photon resonant

The measured and fitted photon counts from each sample and the SHG components are summarized in Table 5.2. For component A_{xxy} the stronger signal is used whenever there is variation in signal levels between angles $\pm 45°$. Overall the results point out that the SHG signals cannot always be predicted theoretically by just looking at whether the input photons couple to a plasmon resonance. The L samples obey the rules about symmetries and resonances but the rest do not. For the T-shaped particles in samples A and B the strongest SHG signal is generated by a component where only one input photon is resonant (A_{xxy}) and the component

with both input photons resonant (A_{yxx}) yields a signal only quarter in strength compared to the highest one. Samples C and D have a component with two resonant photons (A_{yxx}) which still generates only a weak SHG signal. Overall these results point out that the SHG signals cannot be explained purely by plasmonic resonances. They also show that illuminating the particles with light of a resonant allowed polarization is not a certain method of generating a high SHG signal, as claimed by some studies [55].

Table 5.3: Measured photon counts scaled with particle area and normalized to the reference sample (arbitrary units).

	xxy		*yyy*		*yxx*	
	final	test	final	test	final	test
L	0.062	0.025	1	0.74	0.12	0.099
A	0.57	0.60	0.081	0.041	0.17	0.13
B	0.46	0.35	0.047	0.032	0.094	0.10
C	2.1	1.2	1.6	0.18	0.14	0.074
D	2.0	2.1	2.0	1.2	0.092	0.18

Both input photons resonant
One input photon resonant

However, we must also consider the SHG signals relative to the amount of material in the samples. This is important since the ratio of signal and volume is crucial for any applications where we want a strong signal with minimum amount of nonlinear material used. Since the particles in all samples have equal thickness we can use particle areas for scaling the signals. The linearly scaled signals are presented in Table 5.3, normalized to the strongest signal from the reference sample. We observe that when we take the amount of nonlinear material within the sample into account the SHG signals from samples C and D are up to twice as strong compared to the L sample. This means our new particle designs are far superior to the conventional L-shape.

Tensor Components

The values of the NRT components were calculated during the fitting and are presented in Table 5.4. We only consider relative values of the components and all values are normalized with each other, with the component A_{yyy} of the L-sample set to value of 1.

We see that only one tensor component, A_{yyy} for sample C, is clearly stronger than the A_{yyy} component for the reference sample. All others are equal or weaker than the dominant component of the L-shaped particles. The reason we observe a

Table 5.4: Relative values of tensor components calculated from fitting parameters. All components are normalized relative to the component A_{yyy} of the L particles in the final sample.

	A_{xxy}		A_{yyy}		A_{yxx}	
	final	test	final	test	final	test
L	0.31	0.26	1	0.88	0.35	0.32
A	0.77	0.79	0.35	0.25	0.55	0.50
B	0.67	0.63	0.22	0.13	0.42	0.46
C	0.81	0.67	1.23	0.50	0.44	0.34
D	0.80	0.80	1.03	1.06	0.25	0.40

Both input photons resonant
One input photon resonant

stronger response with x-output from T-shaped particles than y-output from L's is that there are always two components A_{xxy} and A_{xyx} influencing the output rather than just one. This means the tensor components don't need to have as large values to obtain high output signals if we can couple the input signal to more than one of them.

5.3 Local Field Distributions

As discussed in the previous chapter, the extinction spectra and plasmonic properties of the samples were not sufficient to explain the measured SHG signals of the studied samples. Another method to account for the results is to examine the local electric fields within the samples when irradiated with the fundamental beam. Since SHG is related to the second power of the field, even small variations in field strength can influence the output signal by a large margin. Especially "hot spots", small areas of extreme field intensity observed within nanostructures can possess field enhancements of more than an order of magnitude which can lead to strong SHG. When any hot spots are present, the SHG signal is often dominated by the their contribution. Hot spots are especially prone to appear within small gaps and sharp corners in the structure, such as the gap area of the T-shapes.

Because measuring the local fields directly is not feasible, numerical simulations were used to calculate local-field distributions for the studied samples. For the local-field calculations FDTD-method was used. The samples were expressed as a 3d-grid composed of uniformly sized cube pixels. The resolution used was 2 nm $\times$ 2 nm *times* 2 nm. According to the structure, each pixel is assigned to a material with specific electromagnetic qualities. Three media were used in the calculations: air (approximated as free space), glass substrate (dielectric) and gold for the particles. Gold was modeled using the Drude-Lorentz model [56]. As with BEM, matching

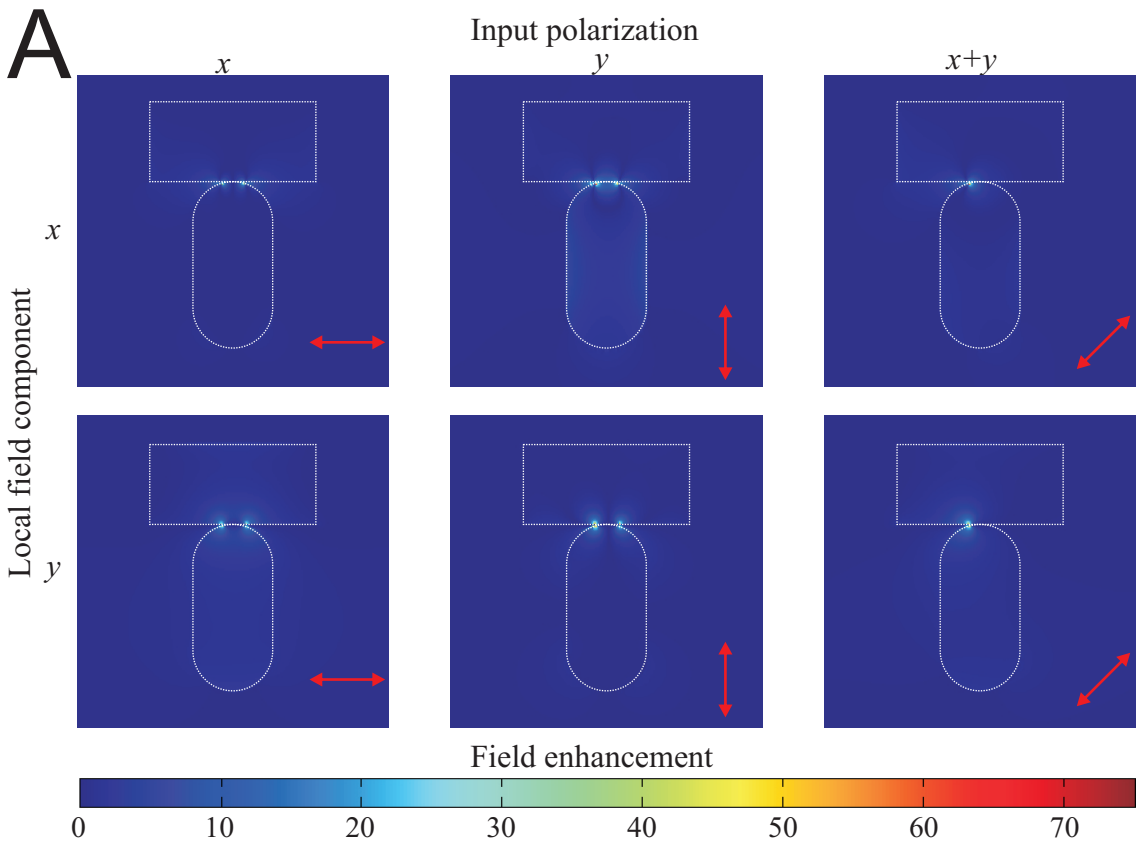

Figure 5.6: Local field distributions for sample A.

field values at the boundaries of the grid accounts for the periodicity. The input signal is modeled as a monochromatic sine wave with a wavelength of 1060 nm, the same as the laser used in the experiments. The local fields are calculated at a plane 10 nm deep from the surface of the sample, in the middle of the particles. Three different polarization states for the input field were used in the calculations. In addition to polarization states aligned with the main axes x and y a third simulation was ran with the input field oscillating at a 45°, called $x+y$ henceforth. This mixed polarization state was seen to be of interest in the previous section because such input polarization yielded the strongest SHG counts.

The simulated local-fields are presented in Figures 5.6 - 5.9. The polarization components x and y of the output field are plotted separately. The values used to generate the images are absolute values of the fields, which means that phase information is not presented. The colors represent field enhancement factor which is local field strength compared to the input field strength. Dark blue areas have almost zero field while light blue spots have enhanced fields. Yellow and red mark areas with hot spots. In each graph the polarization state of the input field is shown with a red arrow and the outline of the particle is shown with a white dashed line. The simulation yields a time-varying result and the phase of the field could be

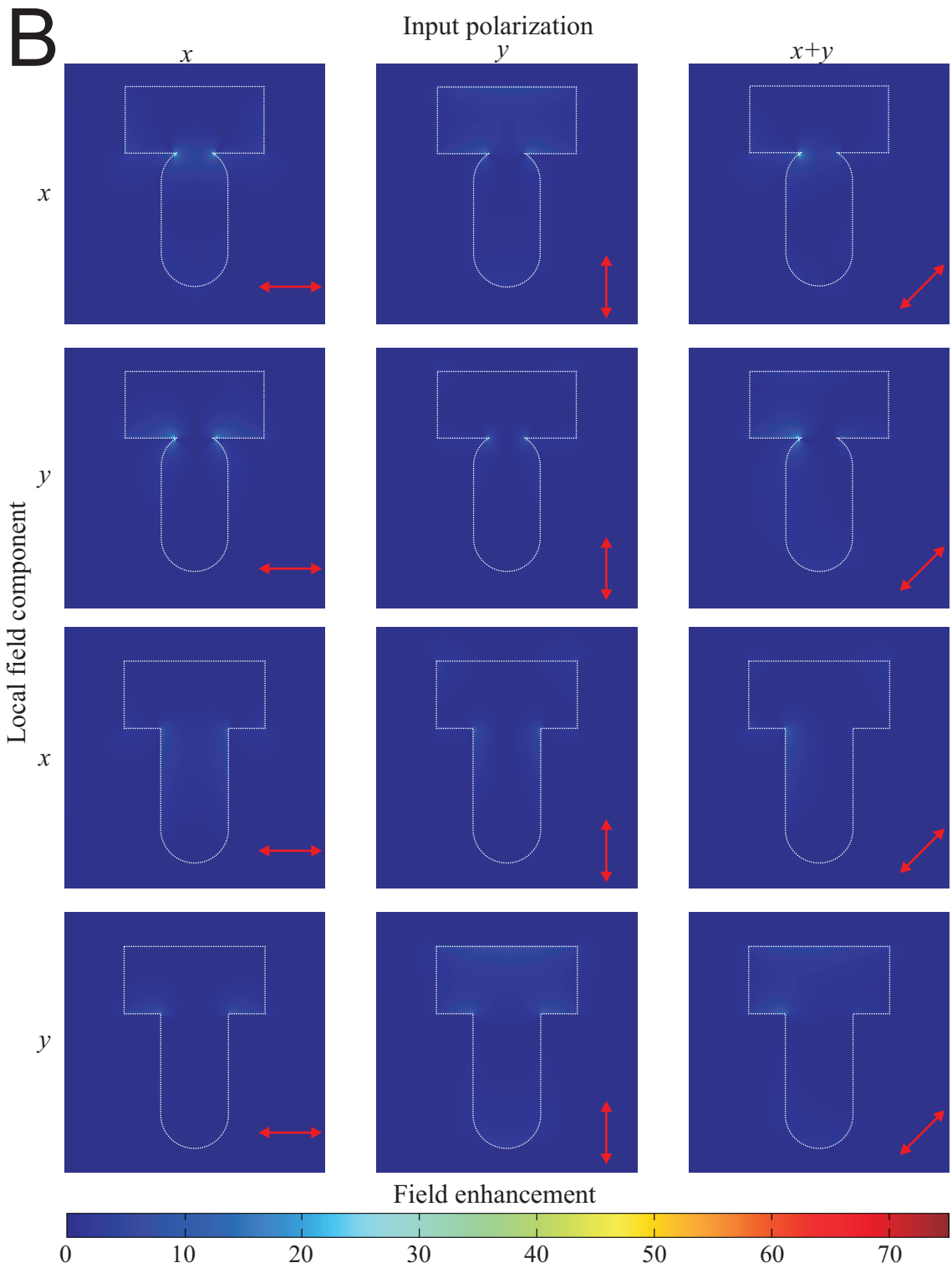

Figure 5.7: Local field distributions for sample B.

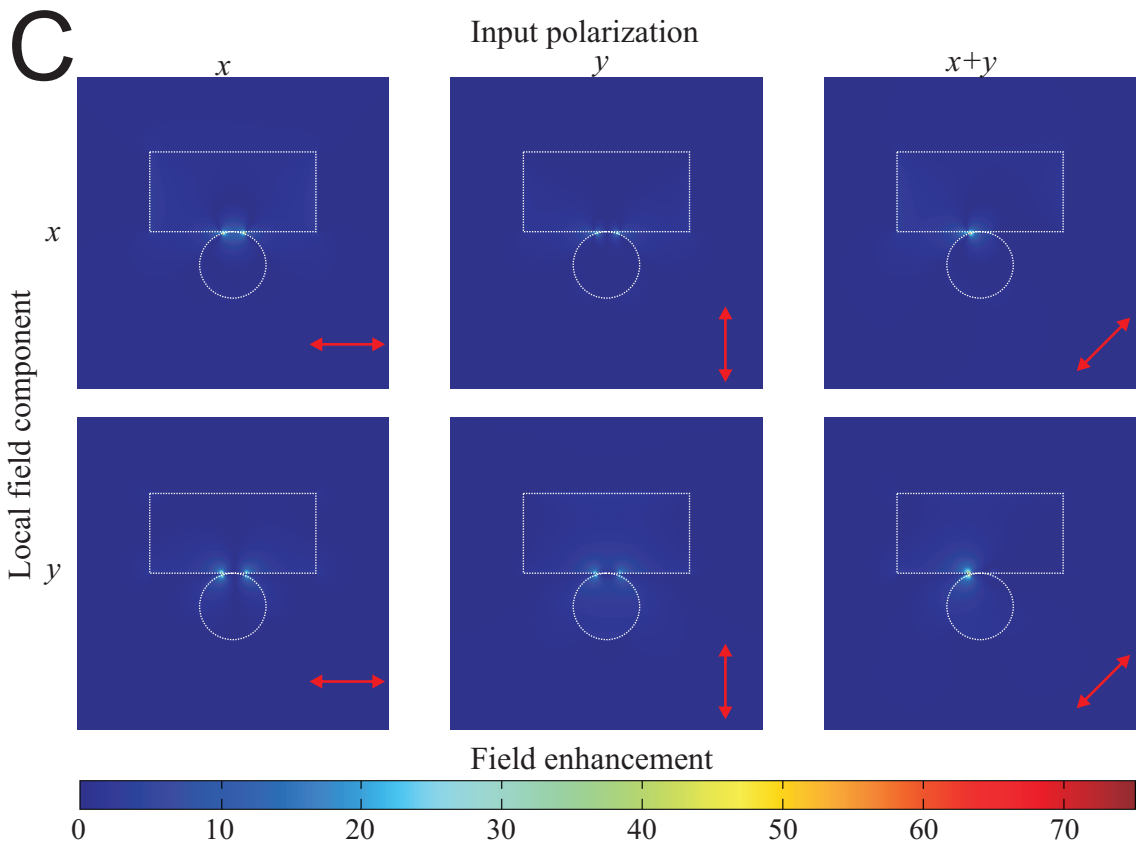

Figure 5.8: Local field distributions for sample C.

changed when plotting the field graph. For all images featured here the phase with the highest field enhancement was chosen. The maximum field enhancements from calculations relevant to SHG are collated in Table 5.5, along with photon counts measured from associated SHG components.

Observations on the Local Fields

As expected, the plotted fields show hot spots within the gaps between the bars that form the particles. The hot spots tend to be stronger when the gap features are sharp (samples A and C) and weaker or almost nonexistent when the particle is approximated without any gap features (sample B). The field enhancements are also influenced by the extinction spectra. When comparing field distributions for y-polarized input for samples B and D, the non-resonant sample (B) displays much weaker local fields.

The local field strengths also reveal why sample A has a stronger SHG yield than sample B despite the latter having a plasmon resonance closer to the laser wavelength. The sharper gap area of sample A results in much stronger field enhancements and hot spots which gives raise to a stronger SHG signal.

An important observation about the local fields is that with both x- and y-

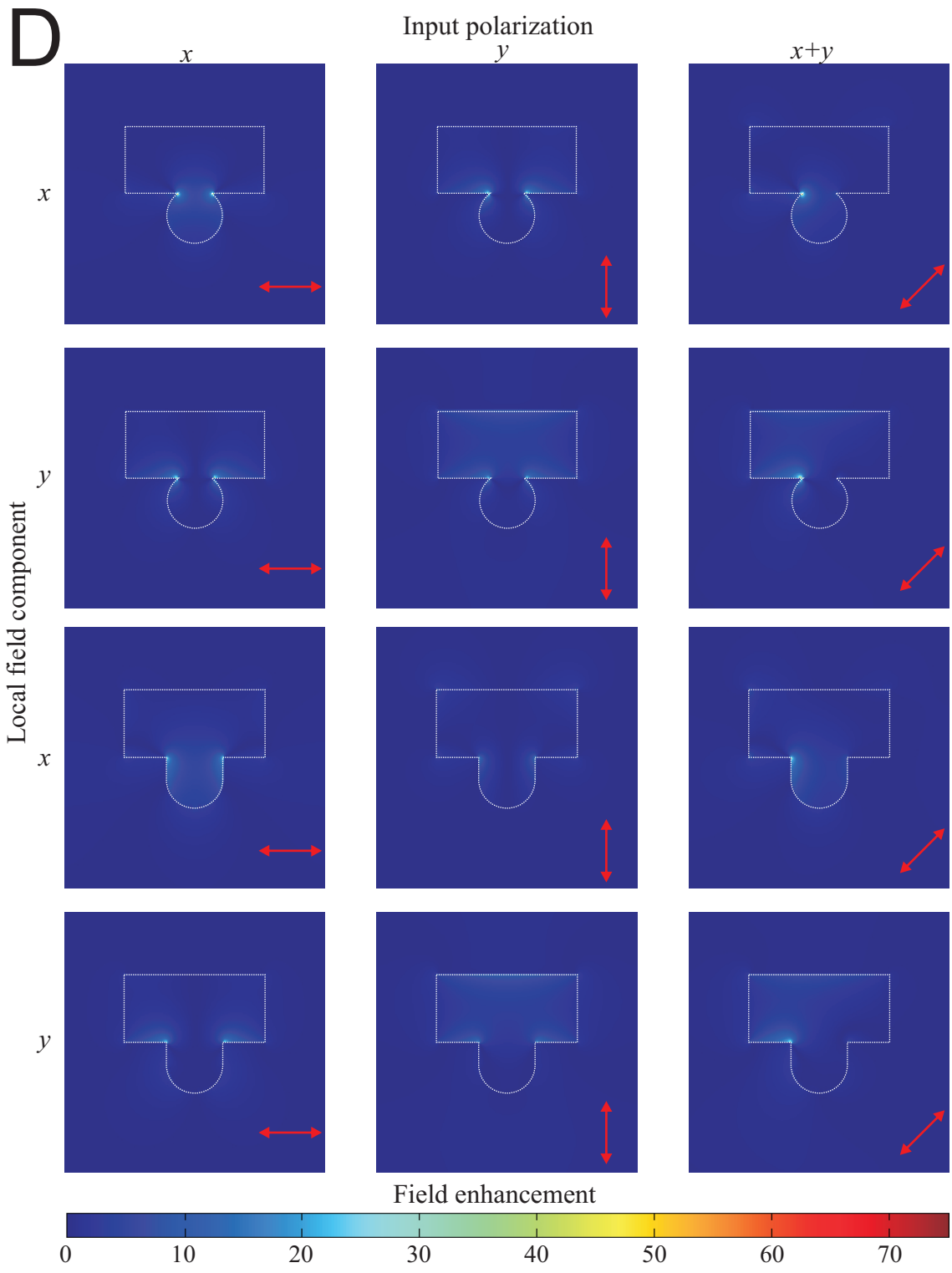

Figure 5.9: Local field distributions for sample D.

Table 5.5: Maximum local field enhancements in the simulations and associated SHG signals for all polarization components.

Sample	Field enhancement (output/input)			SHG signals		
	y/x	y/y	$x/x+y$	yxx	yyy	xxy
A	52	39	54	600	280	1970
B (gap)	35	21	43	320	160	1570
B (no gap)	14	16	16			
C	42	32	61	320	3670	4800
D (gap)	40	30	54	210	4460	4530
D (no gap)	32	21	34			

polarized input fields there are two hot spots but with the mixed polarization state $x+y$ there is only one. The other one is not present or at least is severely weakened. Since $x+y$ is a superposition of the two other polarization states this can be explained through phases of the hot spots. When the input field is y-polarized the particle is symmetric related to the field and thus both hot spots must be at the same phase (Fig. 5.10a). This is not the case for x-polarized light and the two hot spots have opposite phases (Fig. 5.10b). When these two fields are superpositioned together, on one side of the T-shape the phase matched hot spots add together and the local field at the hot spot should be even stronger. The hot spots with opposite phases cancel each other at least partially. The local field is weaker and the hot spot disappears.

By looking at the maximum field enhancements in Table 5.5, we observe that the previous deduction indeed holds true for several samples. The polarization component of the local field associated with allowed SHG at the hot spot is stronger in the $x+y$ -polarized case than with either pure input polarization. The field enhancement for the mixed input polarization is up to 45% stronger than the strongest field enhancement observed with a resonant pure polarization. On average the difference in field enhancement is about 20%. This could explain why SHG gain was measured to be highest from the mixed component xxy. Because SHG scales to the second power of the field, having only one but stronger hot spot could result in more SHG output. However, for the samples where this was the case (A and B) only sample B has a significant difference in local-field strength (23%) between components xxy and yxx. For sample A the difference is negligible which means this approach alone is not enough to explain the difference.

The phase behavior also explains why we observe weak signals for component yxx from samples C and D despite having a resonance and a strong hot spots for the component. Because the input field is x-polarized these hot spots have opposite phases (Fig. 5.10a) and as such any output radiation generated by them tends to interfere destructively in in the far-field. This results in a weak signal despite favorable resonance and symmetry conditions. However, in a previous study, L-

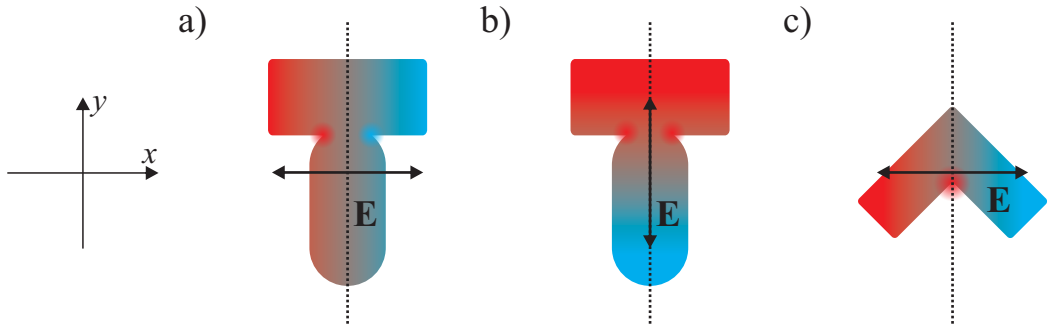

Figure 5.10: Two symmetrical hot spots tend to have a) opposite phase when the field is x-polarized and b) identical phase when the field is y-polarized. c) The L-shape has only one main hot spot.

samples have been designed to resonance match with the laser for such a component and those produced very high SHG signal [53]. Thus it would seem strange that such a component can produce strong SHG from L-shaped particles when they have the same symmetry properties as the T-shape. The difference can be explained by the locations of the hot spots in the L-shape. Similar to the T-shape the L-particles have hot spots along the edges, ends and corners of the arms but SHG from these is negated due to the previous symmetry argument. However, the L has another hot spot in the middle of the shape, along the symmetry axis (Fig. 5.10c), which is not affected by the symmetry rules and can produce SHG [11]. Similar results to our T-shaped particles, where allowed SHG signals are silenced by sample symmetry have also been observed earlier [57].

6. CONCLUSIONS

"I may not have gone where I intended to go, but I think I have ended up where I needed to be."

- Douglas Adams

In summary, both linear and nonlinear optical properties of T-shaped gold nanoparticles were studied in this work. The results were compared to a reference sample of L-shaped particles similar to samples studied a lot in earlier work. To support experimental data we performed numerical simulations using FDTD and BEM methods.

For sample designs we had two different kinds of T-shaped particles: one composed of a rectangular horizontal bar (top) and vertical bar with rounded ends (bottom) and another where the lower bar was replaced with a dot. For both designs we had two variations where the two components either touch each other at one point or overlap by 10 nm. Although the components are connected and form one particle, there are still sharp gap features between them.

The results from linear measurements were close to what we expected. We measured the extinction spectra of the samples and observed resonance peaks near wavelengths which the particles were designed to be resonant with. We observed some unexpected resonances but those were at wavelengths far from the laser wavelength used in the nonlinear experiments and therefore unimportant concerning the rest of the work.

The BEM simulations on linear spectra did not agree too well with the experiment for the most part. Partly this was expected since the model had some simplifications and some samples were known to be challenging to simulate with the method used. Generally the simulated spectra were of similar shape to the measured ones, but the resonance peaks were redshifted compared to the measured peaks. Nevertheless, we were able to determine that the overlapping T-design was better modeled as a mushroom shape without a gap area.

In the nonlinear part we measured SHG with a 1060 nm IR-laser and rotated the input polarization. The goal was to determine the components of the nonlinear response tensor which is related to the nonlinear susceptibility. We observed expected results from our reference sample which fulfilled the symmetry rules estab-

lished before: an allowed SHG component resonant with the input field yields a high signal, otherwise the SHG signal is weak. However, the T-particle samples did not follow this rule. There were cases with resonant allowed signals, yet the measured signals were still weak. Although in those cases the polarization state was different for input and output fields this should not be an issue since such signals have been measured to be strong for L-shaped particles earlier. Surprisingly, we measured strongest signals from mixed polarization components, where the two input photons have different polarization states.

In order to explain the results from SHG measurements, we ran FDTD simulations to calculate the local-field distributions within the samples at the laser wavelength. The main goal of these simulations was to determine the behavior of hot spots, areas of extreme field enhancement within the particles. For the T-particles these tend to form symmetrically within the gap features. Depending on the polarization state of incident light these hot spots can have identical or opposite phases which affects how the output signal interferes at the far-field. This explains why some of the allowed and resonant SHG components were weak. When the field distribution is antisymmetric, any SHG generated interferes destructively and the output signal dies out.

Another phenomenon that was observed in the local-fields was that with a mixed input polarization the hot spots associated with each pure polarization component interfere in the near-field. On one side of the particle the phases of the hot spots match and they merge into a much stronger hot spot. On the other side of the particle the hot spots have opposite phases and they cancel out. This breaks the symmetry of the non phase-matched local-field and enables SHG. The singular hot spot is also stronger than either of the original ones which further enhances SHG which is proportional to the square of the field. This effect was observed in the simulations but not for all samples which had a large difference in SHG signal levels.

Overall we were able to show that our T-shaped particle design is superior to the previously studied L-particles when it comes to SHG signal compared to particle volume. Combined with the fact that the new samples were able to generate SHG from more than one combination of polarization states could make the design useful in applications where high SHG signals are needed with minimal amount of NL material. The results challenge the claim that all you need for high SHG signal is a resonance at the input frequency and an allowed SHG component. Symmetric hot spot locations can silence some components or amplify SHG with mixed input polarization.

Further research on the topic is required. In addition to further varying particle dimensions, we could look into T-dimer samples with nanoscale gaps fabricated between the components. Such samples were already fabricated with a 10 nm gap

but the gap turned out to be too large and no significant SHG was measured. We have concluded that the gaps should be only a few nm in width which makes sample preparation challenging. In terms of research methods, a different laser could be used to couple the input field to the resonances observed at 760 nm. The numerical models are also being developed to include SHG simulations in the future.

REFERENCES

[1] H. Husu. *Electromagnetic Resonances and Local Fields in the Linear and Nonlinear Optical Response of Metal Nanostructures.* Ph.D Thesis 1008. Tampere University of Technology (2011).

[2] F. Wang. *Multipolar Nonlinear Optics of Surfaces and Bulk Materials.* Ph.D Thesis 898. Tampere University of Technology (2010).

[3] M. Huttunen, G. Bautista, M. Decker, S. Linden, M. Wegener, and M. Kauranen. *Nonlinear Chiral Imaging of Subwavelength-Sized Twisted-Cross Gold Nanodimers.* Optical Materials Express, Vol. **1**, 46 (2011).

[4] G. Bautista, M. Huttunen, J. Mäkitalo, J. M. Kontio, J. Simonen, and M. Kauranen. *Second-Harmonic Generation Imaging of Metal Nano-Objects with Cylindrical Vector Beams.* Nano Letters **12**, 3207 (2012).

[5] A. Priimagi, K. Ogawa, M. Virkki, J. Mamiya, M. Kauranen, and A. Shishido. *High-Contrast Photoswitching of Nonlinear Optical Response in Crosslinked Ferroelectric Liquid-Crystalline Polymers.* Advanced Materials **24**, 6410 (2012).

[6] J. Makitalo, S. Suuriniemi, and M. Kauranen. *Boundary Element Method for Surface Nonlinear Optics of Nanoparticles.* Optics Express **19**, 23386 (2011).

[7] A. Boltasseva, V. M. Shalaev. *Fabrication of Optical Negative-Index Metamaterials: Recent Advances and Outlook.* Metamaterials **2**, 1 (2008).

[8] J. Harra, J. Mäkitalo, R. Siikanen, M. Virkki, G. Genty, T. Kobayashi, M. Kauranen, and J. M. Mäkela. *Size-Controlled Aerosol Synthesis of Silver Nanoparticles for Plasmonic Materials.* Journal of Nanoparticle Research **14**, 870 (2012).

[9] J. A. Sioss, and C. D. Keating. *Batch Preparation of Linear Au and Ag Nanoparticle Chains via Wet Chemistry.* Nano Letters **5**, 1779 (2005).

[10] B. K. Canfield, H. Husu, J. Laukkanen, B. Bai, M. Kuittinen, J. Turunen, and M. Kauranen. *Local Field Asymmetry Drives Second-Harmonic Generation in Noncentrosymmetric Nanodimers.* Nano Letters **7**, 1251 (2007).

[11] H. Husu, J. Mäkitalo, J. Laukkanen, M. Kuittinen, and M. Kauranen. *Particle Plasmon Resonances in L-shaped Gold Nanoparticles.* Optics Express **18**, 16601 (2010).

[12] M. W. Klein, C. Enkrich, M. Wegener, C. M. Soukoulis, and S. Linden. *Single-Slit Split-Ring Resonators at Optical Frequencies: Limits of Size Scaling.* Optics Letters **31**, 1259 (2006).

[13] S.J Oldenburg, R.D Averitt, S.L Westcott, and N.J Halas. *Nanoengineering of Optical Resonances*. Chemical Physics Letters **288**, 243 (1998).

[14] J. B. Pendry. *Negative Refraction*. Contemporary Physics **45**, 191 (2004).

[15] J. B. Pendry. *Negative Refraction Makes a Perfect Lens*. Physical Review Letters **85**, 3966 (2000).

[16] T. Ergin, N. Stenger, P. Brenner, J. B. Pendry, and M. Wegener. *Three-Dimensional Invisibility Cloak at Optical Wavelengths*. Science **16**, 337 (2010).

[17] P. Mühlschlegel, H.-J. Eisler, O. J. F. Martin, B. Hecht, and D. W. Pohl. *Resonant Optical Antennas*. Science **10**, 1607 (2005).

[18] S. Zou, and G. C. Schatz. *Silver Nanoparticle Array Structures that Produce Giant Enhancements in Electromagnetic Fields.* Nature **453**, 757 (2008).

[19] H. Tuovinen, M. Kauranen, K. Jefimovs, P. Vahimaa, T. Vallius, J. Turunen, N. Tkachenko, and H. Lemmetyinen. *Linear and Second-Order Nonlinear Optical Properties of Arrays of Noncentrosymmetric Gold Nanoparticles*. Journal of Nonlinear Optical Physics & Materials **11**, 421 (2002).

[20] R. Czaplicki, M. Zdanowicz, K. Koskinen, J. Laukkanen, M. Kuittinen, and M. Kauranen. *Dipole Limit in Second-harmonic Generation from Arrays of Gold Nanoparticles*. Optics Express **19**, 26866 (2011).

[21] E. Hecht. *Optics*. 3rd edition. Addison Wesley (1998).

[22] R. W. Boyd. *Nonlinear Optics*. 2nd edition. Academic Press (2003).

[23] M. Born, E. Wolf. *Principles of Optics*. 2nd edition. Pergamon Press (1986).

[24] C. F. Bohren, D. R. Huffman. *Absorption and Scattering of Light by Small Particles*. Wiley Science. (1983).

[25] J. M. Hollas. *Modern Spectroscopy*. 4th edition, John Wiley & Sons, Ltd (2004).

[26] P. A. Franken, A. E. Hill, C. W. Peters, and G. Weinreich. *Generation of Optical Harmonics*. Physical Review Letters **7**, 118 (1961).

[27] Y. R. Shen. *The Principles of Nonlinear Optics*. Wiley Interscience. (1984).

[28] C. M. Soukoulis, S. Linden, M. Wegener. *Negative Refractive Index at Optical Wavelengths*. Science **5**, 47 (2007).

[29] V. M. Shalaev. *Optical Negative-Index Metamaterials*. Nature Photonics **1**, 41 (2007).

[30] C. M. Soukoulis, and M. Wegener. *Past Achievements and Future Challenges in the Development of Three-Dimensional Photonic Metamaterials.* Nature Photonics **5**, 523 (2011).

[31] G. V. Eleftheriades, and K. G. Balmain. *Negative-Refraction Metamaterials, Fundamental Principles and Applications.* John Wiley & Sons Inc. (2005).

[32] H. P. Myers. *Introductory Solid State Physics.* 2nd edition. CRC Press. (1997).

[33] C. J. Powell, and J.B. Swan. *Origin of the Characteristic Electron Energy Losses in Aluminum.* Physical Review **115**, 869 (1959).

[34] W. L. Barnes, A. Dereux and T. W. Ebbesen. *Surface Plasmon Subwavelength Optics.* Nature **424**, 824 (2003).

[35] J. R. Krenn, H. Ditlbacher, G. Schider, A. Hohenau, A. Leitner, F. R. Aussenegg. *Surface Plasmon Micro- and Nano-Optics.* Journal of Microscopy **209**, 167 (2002).

[36] T. Holmgaard, S. I. Bozhevolnyi, L. Markey, A. Dereux, A. V. Krasavin, P. Bolger, and A. V. Zayats. *Efficient Excitation of Dielectric-Loaded Surface Plasmon-Polariton Waveguide Modes at Telecommunication Wavelengths.* Physical Review B **78**, 165431 (2008).

[37] P. Neuzil and J. Reboud. *Palm-Sized Biodetection System Based on Localized Surface Plasmon Resonance.* Analytical Chemistry **80**, 6100 (2008).

[38] S. A. Maier. *Plasmonics.* Springer Science (2007).

[39] G. Mie. *Beiträge zur Optik trüber Medien, speziell kolloidaler Metallösungen.* Annalen der Physik **330**, 337 (1908).

[40] D. A. Genov, A. K. Sarychev, V. M. Shalaev, and A. Wei. *Resonant Field Enhancements from Metal Nanoparticle Arrays.* Nano Letters **4**, 153 (2004).

[41] S. Kim, J. Jin, Y.-J. Kim, I.-Y. Park, Y. Kim and S.-W. Kim. *High-Harmonic Generation by Resonant Plasmon Field Enhancement.* Nature **453**, 757 (2008).

[42] G. B. Arfken, H. J. Weber. *Mathematical Methods for Physicists.* 5th edition. Academic Press (2001).

[43] S. Kujala, B. K. Canfield, M. Kauranen, Y. Svirko and J. Turunen. *Multipole Interference in the Second-Harmonic Optical Radiation from Gold Nanoparticles.* Physical Review Letters **98**, 167403 (2007).

[44] H. Husu, R. Siikanen, J. Lehtolahti, J. Laukkanen, M. Kuittinen, M. Kauranen. *Metamaterials with Tailored Nonlinear Optical Response*. Nano Letters **12**, 673 (2012).

[45] C. Vieu, F. Carcenac1, A. Pépin, Y. Chen, M. Mejias, A. Lebib, L. Manin-Ferlazzo, L. Couraud, and H. Launois. *Electron Beam Lithography: Resolution Limits and Applications*. Applied Surface Science **164**, 111 (2002).

[46] A. Grigorescu, M. C. van der Krogt, C. Hagen, and P. Kruit. *10 nm Lines and Spaces Written in HSQ, Using Electron Beam Lithography*. Microelectronic Engineering **84**, 822 (2007).

[47] H. Husu, J. Mäkitalo, R. Siikanen, G. Genty, H. Pietarinen, J. Lehtolahti, J. Laukkanen, M. Kuittinen and M. Kauranen. *Spectral Control in Anisotropic Resonance-Domain Metamaterials*. Optics Letters **36**, 2375 (2011).

[48] A. Taflove. *Application of the Finite-Difference Time-Domain Method to Sinusoidal Steady-State Electromagnetic-Penetration Problems*. IEEE Transactions on Electromagnetic Compatibility **22**, 191 (1980).

[49] D. H. Choi, and W. J. R. Hoefer. *Application of the Finite-Difference Time-Domain Method to Sinusoidal Steady-State Electromagnetic-Penetration Problems*. IEEE Transactions on Microwave Theory and Technique **34**, 1464 (1986).

[50] S. Kagami, and I. Fukai. *Application of Boundary-Element Method to Electromagnetic Field Problems*. IEEE Transactions on Microwave Theory and Technique **32**, 455 (1984).

[51] A. Taflove, S. C. Hagness. *Computational Electrodynamics: The Finite-Difference Time-Domain Method*. 3rd edition. Artech House (2005).

[52] *Introduction to the Boundary Element Method*. www.boundary-element-method.com

[53] R. Czaplicki, H. Husu, R. Siikanen, J. Mäkitalo, M. Kauranen, J. Laukkanen J. Lehtolahti, and M. Kuittinen. *Enhancement of Second-Harmonic Generation from Metal Nanoparticles by Passive Elements*. Physical Review Letters **110**, 093902 (2013).

[54] H. Husu. *Optical Characterization of T-shaped Gold Nanodimers*. M.Sc Thesis. Tampere University of Technology (2007).

[55] F. B. P. Niesler, N. Feth, S. Linden, and M. Wegener. *Second-Harmonic Optical Spectroscopy on Split-Ring Resonator Arrays*. Optics Letters **36**, 1533 (2011).

[56] A. Vial, A.-S. Grimault, D. Macias, D. Barchiesi, and M. L. de la Chapelle. *Improvement Analytical Fit of Gold Dispersion. Application to the Modeling of Extinction Spectra with a Finite-difference-time-domain Method.* Physical Review B **71**, 085416 (2005).

[57] J. Berthelot, G. Bachelier, M. Song, P. Rai, G. C. des Francs, A. Dereux, and A. Bouchelier. *Silencing and Enhancement of Second-Harmonic Generation in Optical Gap Antennas.* Optics Express **20**, 10498 (2012).